

High resolution observations of ^{12}CO and $^{13}\text{CO } J = 3 \rightarrow 2$ toward the NGC 6334 extended filament

I. Emission morphology and velocity structure

S. Neupane¹, F. Wyrowski¹, K. M. Menten¹, J. Urquhart², D. Colombo^{1,3}, L.-H. Lin¹, and G. Garay⁴

¹ Max-Planck-Institut für Radioastronomie, Auf dem Hügel 69, 53121 Bonn, Germany
e-mail: sneupane@mpi.fr-bonn.mpg.de

² Centre for Astrophysics and Planetary Science, University of Kent, Canterbury, CT2 7NH, UK

³ Argelander-Institut für Astronomie, Auf dem Hügel 71, 53121 Bonn

⁴ Departamento de Astronomia, Universidad de Chile, Casilla 36-D, Santiago, Chile

Received 2024; accepted 2024

ABSTRACT

NGC 6334 is a giant molecular cloud (GMC) complex that exhibits elongated filamentary structure and harbours numerous OB-stars, H II regions and star forming clumps. To study the emission morphology and velocity structure of the gas in the extended NGC 6334 region using high-resolution molecular line data, we made observations of the ^{12}CO and $^{13}\text{CO } J = 3 \rightarrow 2$ lines with the LAsMA instrument at APEX telescope. The LAsMA data provided a spatial resolution of $20''$ (~ 0.16 pc) and sensitivity of 0.4 K at a spectral resolution of 0.25 km s⁻¹. Our observations revealed that gas in the extended NGC 6334 region exhibits connected velocity coherent structure over ~ 80 pc parallel to the galactic plane. The NGC 6334 complex has its main velocity component at ~ -3.9 km s⁻¹ with two connected velocity structures at velocities ~ -9.2 km s⁻¹ (the ‘bridge’ features) and ~ -20 km s⁻¹ (the Northern Filament, NGC 6334-NF). We observed local velocity fluctuations at smaller spatial scales along the filament that are likely tracing local density enhancement and infall while the broader V-shaped velocity fluctuations observed toward the NGC 6334 central ridge and G352.1 region located in the eastern filament EF1 indicate globally collapsing gas onto the filament. We investigated the ^{13}CO emission and velocity structure around 42 WISE H II regions located in the extended NGC 6334 region and found that most H II regions show signs of molecular gas dispersal from the center (36 of 42) and intensity enhancement at their outer radii (34 of 42). Furthermore most H II regions (26 of 42) are associated with least one ATLASGAL clump within or just outside of their radii the formation of which may have been triggered by H II bubble expansion. Typically toward larger size H II regions we found visually clear signatures of bubble shells emanating from the filamentary structure. Overall the NGC 6334 filamentary complex exhibits sequential star formation from west to east. Located in the west, the GM-24 region exhibits bubbles within bubbles and is at a relatively evolved stage of star formation. The NGC 6334 central ridge is undergoing global gas infall and exhibits two gas ‘bridge’ features possibly connected to the cloud-cloud collision scenario of the NGC 6334-NF and the NGC 6334 main gas component. The relatively quiescent eastern filament (EF1 - G352.1) is a hub-filament in formation which shows the kinematic signature of global gas infall onto the filament. Our observations highlight the important role of H II regions in shaping the molecular gas emission and velocity structure as well as the overall evolution of the molecular filaments in the NGC 6334 complex.

Key words. stars: formation – ISM: structure – ISM: clouds – ISM: kinematics and dynamics – ISM: HII regions – submillimeter:ISM

1. Introduction

NGC 6334 is a giant molecular cloud (GMC) complex, harbouring a central dense filament and a large number of OB-type stars, H II regions/bubbles and star forming clumps in the extended region (e.g., Loughran et al. 1986; Kraemer & Jackson 1999; Muñoz et al. 2007; Persi & Tapia 2008; André et al. 2016; Russeil et al. 2013; Tigé et al. 2017; Arzoumanian et al. 2022). This complex is located at a distance of ~ 1.7 kpc (e.g., Russeil et al. 2012) and its large-scale molecular appearance is dominated by a ~ 70 pc long filamentary structure (within $352.6 \geq l \geq 350.2$ (where l is Galactic longitude). The central dense ridge of NGC 6334, extending along the filament, contains sites of high-mass star formation in a sequence of evolutionary stages (e.g, Tigé et al. 2017) and has been reported to be undergoing longitudinal collapse, possibly triggered by a past high-mass star forming event (e.g., Zernickel et al. 2013; Russeil et al. 2013). Arzouma-

nian et al. (2022) studied the extended NGC 6334 region based on their ^{13}CO and $\text{C}^{18}\text{O } J = 2 \rightarrow 1$ observations obtained with the APEX telescope and highlighted cases of multiple gas compression in the region. In addition, they found a large number of velocity coherent filaments (VCFs) and interpreted their formation resulting from large-scale compression by propagating shock fronts. Presenting a broader picture Fukui et al. (2018b) proposed a cloud-cloud collision scenario in which a collision is happening from lower to higher longitudes of the extended NGC 6334 region, giving rise to the evolutionary sequence of star formation. A similar evolutionary sequence from lower longitude (GUM 1-24) to higher (in the NGC 6334 extended filament) is also reported by Russeil et al. (2013).

The formation of the large scale filaments and their fragmentation processes are not understood well (see the review by Hacar et al. 2023). High angular resolution continuum and molecular line observations are essential to understand the small to large

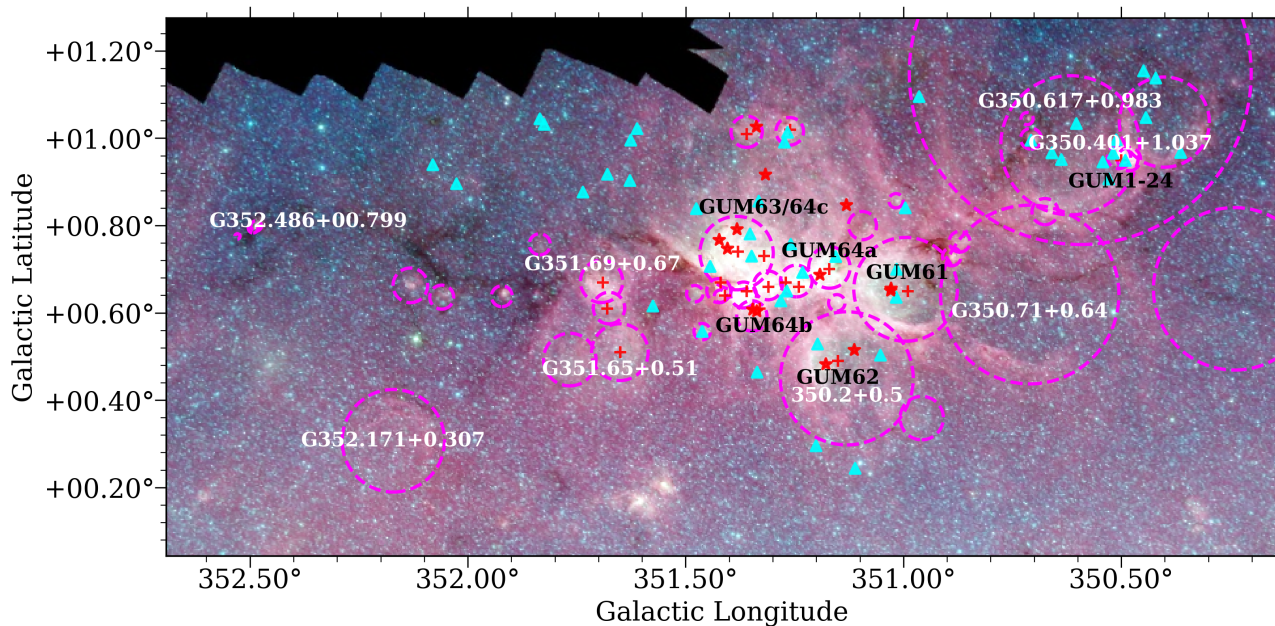


Fig. 1: Spitzer three color image (Red: $8 \mu\text{m}$, Green: $4.5 \mu\text{m}$, Blue: $3.6 \mu\text{m}$) of the NGC 6334 extended region. OB stars from [Russeil et al. \(2020\)](#) and [Persi & Tapia \(2008\)](#) are indicated by cyan triangles and red stars, respectively. H II bubbles from [Anderson et al. \(2014\)](#) are shown by dotted magenta circles, some of which are labelled in white/black text. Plus red markers show positions of radio sources from [Russeil et al. \(2017\)](#).

scale gas kinematics through which gas flows along or onto the filament. Regarding the formation of molecular clouds in the filaments, [Elmegreen \(1998\)](#) have highlighted the important role of gas compression due to H II regions (see also [Inutsuka et al. 2015](#)). H II regions are signposts of (high-mass) star formation within molecular clouds (e.g., [Churchwell 2002](#)). New H II regions are formed inside proto-stellar cores forming high mass stars (OB-type) and their influence is evident on the evolution of the cloud as they emerge. At evolved stages, H II regions can shape the parental cloud material into structures with bubble- or shell-like morphology, in which triggered cases of star formation can proceed (cf. [Elmegreen 1998](#)). The young and evolved H II regions, either found in isolation or in groups, shape the gas emission and velocity structure around them, therefore, their role in natal cloud dispersal and in creating a new generation of star formation requires detailed observational study of the gas kinematics around them.

The extended NGC 6334 region (including GM-24) (see Figure 1) contains 42 infrared H II regions/bubbles reported in the catalog¹ of [Anderson et al. \(2014\)](#), of which 14 are classified as ‘known’ (K), 9 as ‘group’ (G), 6 as ‘candidate’ (C) and 13 as ‘radio quiet’ (Q) H II regions. Identification of these regions were primarily based on the mid-infrared characteristics of the WISE all sky survey data (see [Anderson et al. 2014](#) for more details) and their sizes range between 0.2 pc to 12 pc (see Table 1).

In this work we aim to study the gas emission morphology and velocity structure of the NGC 6334 extended region using high-resolution observations of ^{12}CO and $^{13}\text{CO } J = 3 \rightarrow 2$ molecular lines obtained with the LAsMA instrument on the APEX Telescope. Our goal is to disentangle, with this new large-scale, sensitive and high resolution spectral line data, the different origins of the velocity structure in NGC 6334. This is done by investigating the impact of a large number of H II regions al-

ready formed in the giant molecular complex as well as the large scale inflow of gas onto and through the filaments.

The paper is organized as follows. In Section 2 we describe the APEX LAsMA observations toward the region and provide an overview of the data reduction process and resulting sensitivities. In Section 3 we present the results. In Section 3.2 we present the velocity structure of the extended filament. In Section 3.3 gas emission properties around the H II sources will be presented. The Sections 4 and 5 will include analysis and discussion of the results. Finally, in Section 6 summarizes highlights of this work.

2. Observations and data reduction

2.1. LAsMA observations of ^{12}CO and $^{13}\text{CO } J = 3 \rightarrow 2$

We mapped the NGC 6334 star forming complex in the $^{12}\text{CO } J = 3 \rightarrow 2$ and $^{13}\text{CO } J = 3 \rightarrow 2$ lines, using the Large APEX sub-Millimetre Array (LAsMA), a 7-pixel heterodyne array receiver installed on the Atacama Pathfinder EXperiment 12 meter submillimeter telescope (APEX) located on the Llano de Chajnantor (elevation of ~ 5100 m) in the Atacama desert, Chile. The LAsMA receiver operates in the $870 \mu\text{m}$ (345 GHz) atmospheric window and its 7-pixels are arranged in a hexagonal shape with one central pixel and $40''$ spacing between pixels, which corresponds to ~ 2 FWHM beam widths. The map was centered at Galactic coordinates $l = 351.415^\circ$ and $b = +0.66^\circ$. The area of the extended NGC 6334 region mapped in this project covers $\sim 2.5^\circ \times 1.2^\circ$.

The observations were made during June to September 2021 under good atmospheric conditions of ≤ 1.5 mm precipitable water vapor (PWV) content. The mapped region was divided into $10' \times 10'$ -sized sub-maps (‘tiles’) that were observed in on-the-fly (OTF) mode in both l and b directions. The $^{12}\text{CO } J = 3 \rightarrow 2$ and $^{13}\text{CO } J = 3 \rightarrow 2$ lines were observed simultaneously using a local oscillator frequency of 338.3 GHz. The $^{13}\text{CO } (\nu_{rest} = 330.587$

¹ WISE catalog V2.2: <http://astro.phys.wvu.edu/wise/>

GHz) line is observed in the lower side band and ^{12}CO ($v_{\text{rest}} = 345.796$ GHz) line in the upper side band. An advanced version of the APEX Fast Fourier Transform Spectrometer (FFTS, Klein et al. 2012) was used as a backend, resulting in a spectral resolution of 0.1 km s^{-1} . At this observing frequency, the full width half maximum (FWHM) beam width of the telescope is $\sim 19''$. The OTF observing time for each tile coverage was ~ 35 minutes and the total time spent to complete this project, including overheads, was approximately ~ 62 hours.

2.2. Data reduction process

Data reduction was performed using the GILDAS² software package. The following steps were taken to obtain the final spectral cubes of the full mapped region: first, we extracted the spectra in the -100 km s^{-1} to $+100 \text{ km s}^{-1}$ LSR velocity range and re-sampled them to a common velocity resolution of 0.25 km s^{-1} . The baseline subtracted data sets from different days and sub regions were then combined to produce spectral cubes for the full mapped region. We use the *table* and *xy_map* packages in CLASS-GILDAS to regrid and smooth the data to the desired pixel size and resolution. The pixel size of the final cubes is set to $6'' \times 6''$, chosen to afford better than Nyquist sampling as well as to match that of other complementary data sets. In this data reduction procedure, we carefully flagged and removed spectra with bad baseline and those that contain ripples and artifacts. The final spatial resolution for the cubes is $20''$, 0.16 pc at the distance of 1.7 kpc .

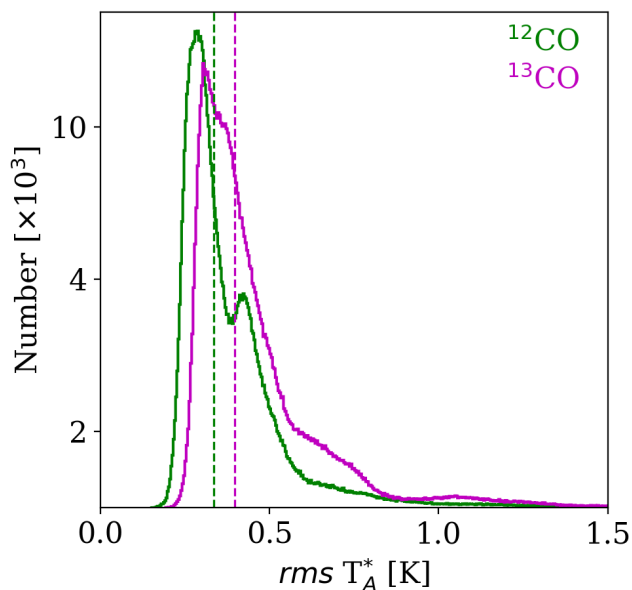


Fig. 2: Histogram of the $\text{rms } T_A^*$ [K] in the ^{13}CO and ^{12}CO lines. The dotted vertical lines in color indicate the median rms values.

2.3. rms sensitivity

Figure 2 presents the histogram of the *root mean square* noise (rms in corrected antenna temperature T_A^* [K])³ for both the ^{13}CO and ^{12}CO spectra estimated from the first order baseline fit to

the spectra. The average rms in T_A^* (computed per channel per pixel at the velocity resolution of 0.25 km s^{-1}) for ^{12}CO and ^{13}CO is 0.39 K and 0.46 K , respectively. The rms distribution of the ^{13}CO emission is presented in Figure A.1. The median rms in T_A^* for ^{12}CO and ^{13}CO is 0.34 K and 0.40 K , respectively. A 3σ detection in ^{13}CO roughly correspond to a column density of $N_{^{13}\text{CO}} \sim 3 \times 10^{14} \text{ cm}^{-2}$ ($N_{\text{H}_2} \sim 2 \times 10^{20} \text{ cm}^{-2}$), estimated with RADEX⁴ assuming a kinetic temperature of 20 K , density (n_{H_2}) of 10^4 cm^{-3} and abundance ratios of $^{12}\text{CO}/^{13}\text{CO}=77$ (Wilson & Rood 1994), $^{12}\text{CO}/\text{H}_2 \sim 8.5 \times 10^{-5}$ (Frerking et al. 1982).

Previous studies of NGC 6334 in the $^{12}\text{CO } J = 2 \rightarrow 1$ line line using the NANTEN2 Telescope had a spectral resolution of $\sim 0.1 \text{ km s}^{-1}$ and rms noise level of $\sim 1.1 \text{ K}$ per channel at an angular resolution of $\sim 90''$ (Fukui et al. 2018b). Furthermore, previous ^{13}CO and $\text{C}^{18}\text{O } J = 2 \rightarrow 1$ observations with APEX had a spectral resolution of 0.3 km s^{-1} and sensitivity of about $\sim 0.5 \text{ K}$ at an angular resolution of $\sim 30''$ covering $2.2^\circ \times 0.7^\circ$ region (see, Arzoumanian et al. 2022). In comparison to both of these previous studies, we have at least 1.5 times higher spatial resolution, better sensitivity and map twice as large an area to cover the extended emission region. In addition, since we observe the higher excitation $^{13}\text{CO } J = 3 \rightarrow 2$ lines, we also probe higher density gas (e.g., $n_{\text{crit}} \sim 1 \times 10^4 \text{ cm}^{-3}$ at 10 K) directly participating in the star forming activity.

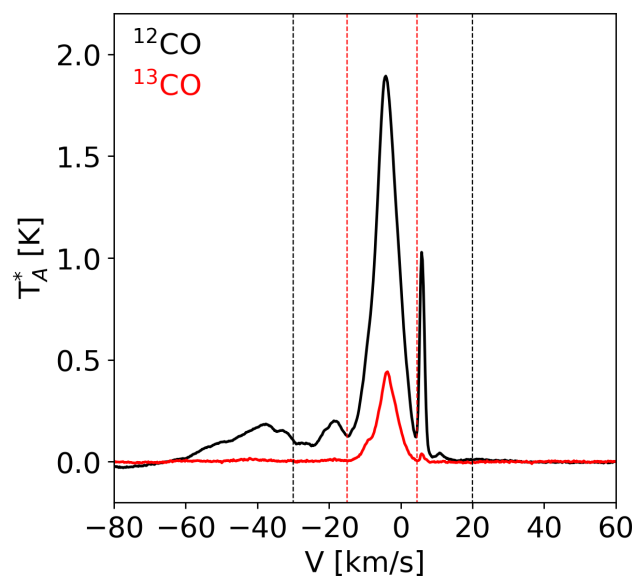


Fig. 3: Average of the ^{13}CO (in red) and ^{12}CO (in black) spectra toward the NGC 6334 extended filament. The vertical dotted lines indicate velocity ranges of $[-30, +20]$ and $[-15, +5] \text{ km s}^{-1}$ in black and red color, respectively.

3. Results

3.1. CO emission morphology

Figure 3 presents the ^{13}CO and $^{12}\text{CO } J = 3 \rightarrow 2$ spectra as in red and black, respectively, averaged over the extended NGC 6334 filament. Most of the ^{13}CO emission is confined within the velocity range of -15 to $+5 \text{ km s}^{-1}$, while ^{12}CO emission is ob-

² <https://www.iram.fr/IRAMFR/GILDAS/>

³ We used antenna temperature units T_A^* throughout this work unless otherwise stated in the text.

⁴ RADEX: Non-LTE molecular radiative transfer in an isothermal homogeneous medium by van der Tak et al. (2007), also available online at <https://personal.sron.nl/~vdtak/radex/index.shtml>

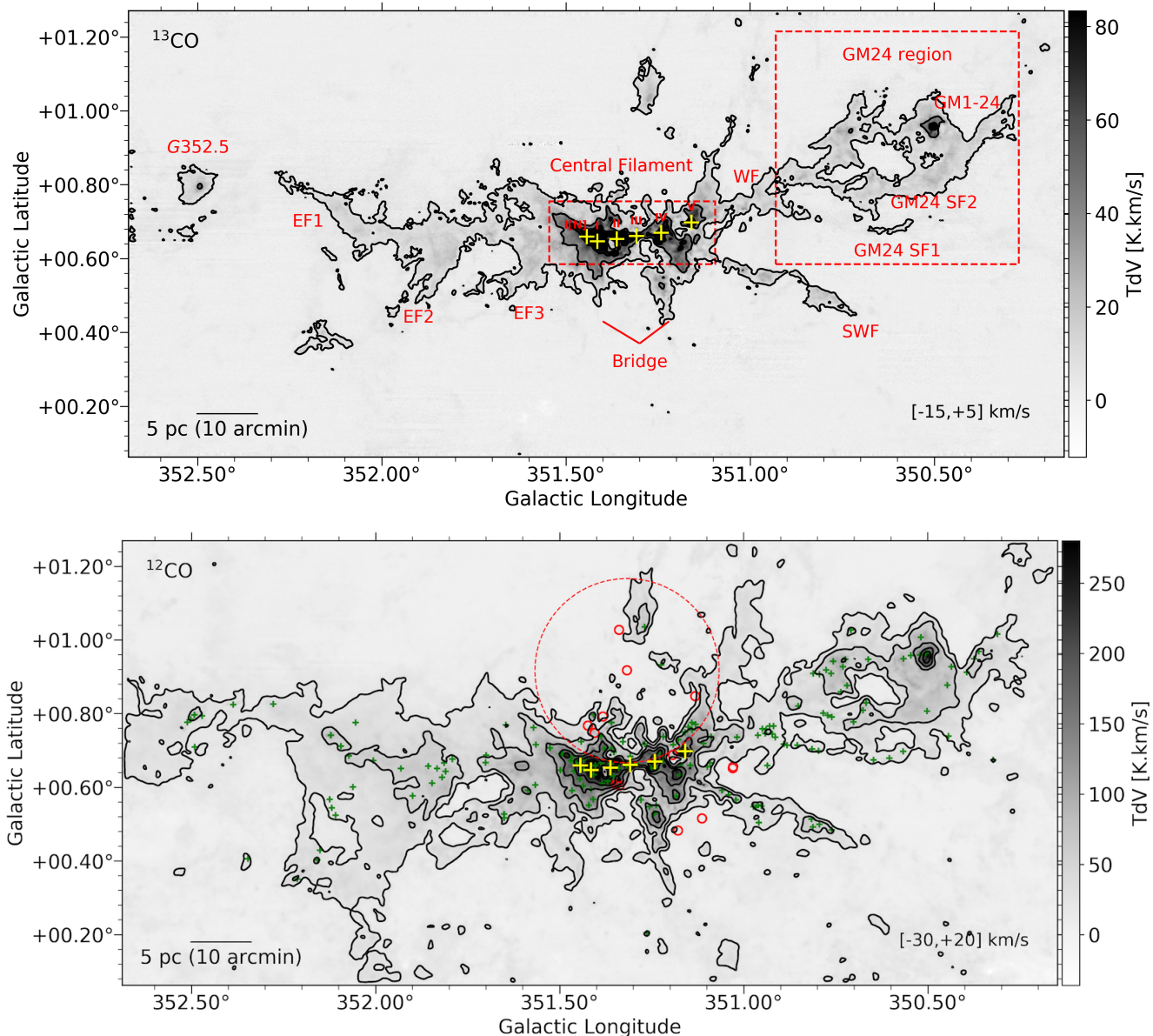


Fig. 4: ^{13}CO (top) and ^{12}CO (bottom) emission morphologies (moment 0 maps) toward the extended NGC 6334 filament. Contours are drawn at 7, 30 and 70 K km s^{-1} for ^{13}CO and at 15, 50, 100, 150 and 200 K km s^{-1} for ^{12}CO . Velocity ranges used for integrating the intensities are given in bottom right corner of the maps. Dashed red boxes in top image outline the central filament and the GM24 region. Various regions discussed in the text are labeled in red. Far-Infrared (FIR) sources I[N], I to V (corresponding to radio sources F to A, see Kraemer & Jackson 1999) are marked with yellow plus markers on the images. In the ^{12}CO moment 0 map also the OB star positions from Persi & Tapia (2008) are shown as red open dots. A circle is drawn centered at $l = 351.317, b = 0.918$, the position of the dominant O6.5 star, to match the arc-like emission morphology observed toward the NGC 6334 central filament. The green plus markers indicate the position of ATLASGAL sources in the NGC 6334 extended region (Urquhart et al. 2018b).

served also at significantly blue-shifted velocities. In both lines, the emission peaks around -4 km s^{-1} , the systemic velocity of the gas in the main filament. In ^{13}CO , a less prominent peak is seen at around -9 km s^{-1} blended with the main component. Another emission peak is seen at a redder velocity of $+7 \text{ km s}^{-1}$ in both lines, which is associated with local molecular clouds (e.g., Russeil et al. 2017). Blue-shifted ^{12}CO emission is found down to -60 km s^{-1} and has two peaks around -20 km s^{-1} and -40 km s^{-1} that do not have clear ^{13}CO counterparts. The -15 to $+5 \text{ km s}^{-1}$ range, corresponding to the bulk of the emission in the ^{13}CO line, is indicated by the dotted red lines and -30 to $+20 \text{ km s}^{-1}$, corresponding to the bulk of the ^{12}CO emission, is indicated

by the dotted black lines in the Figure 3. We use these velocity ranges to compute the moment 0 maps.

Figure 4 presents the ^{13}CO (top panel) and ^{12}CO (bottom panel) velocity integrated moment 0 maps of the extended NGC 6334 filament. The prominent features discussed in the text are also labelled in the top panel image. Also indicated in the figure are the OB stars from Persi & Tapia (2008) (red circles) and ATLASGAL clumps from Urquhart et al. (2018b) (green plus markers).

The morphology of the CO line emission shows that the NGC 6334 central filament has a spatially concentrated dense gas reservoir. In both CO lines, the central filament is generally

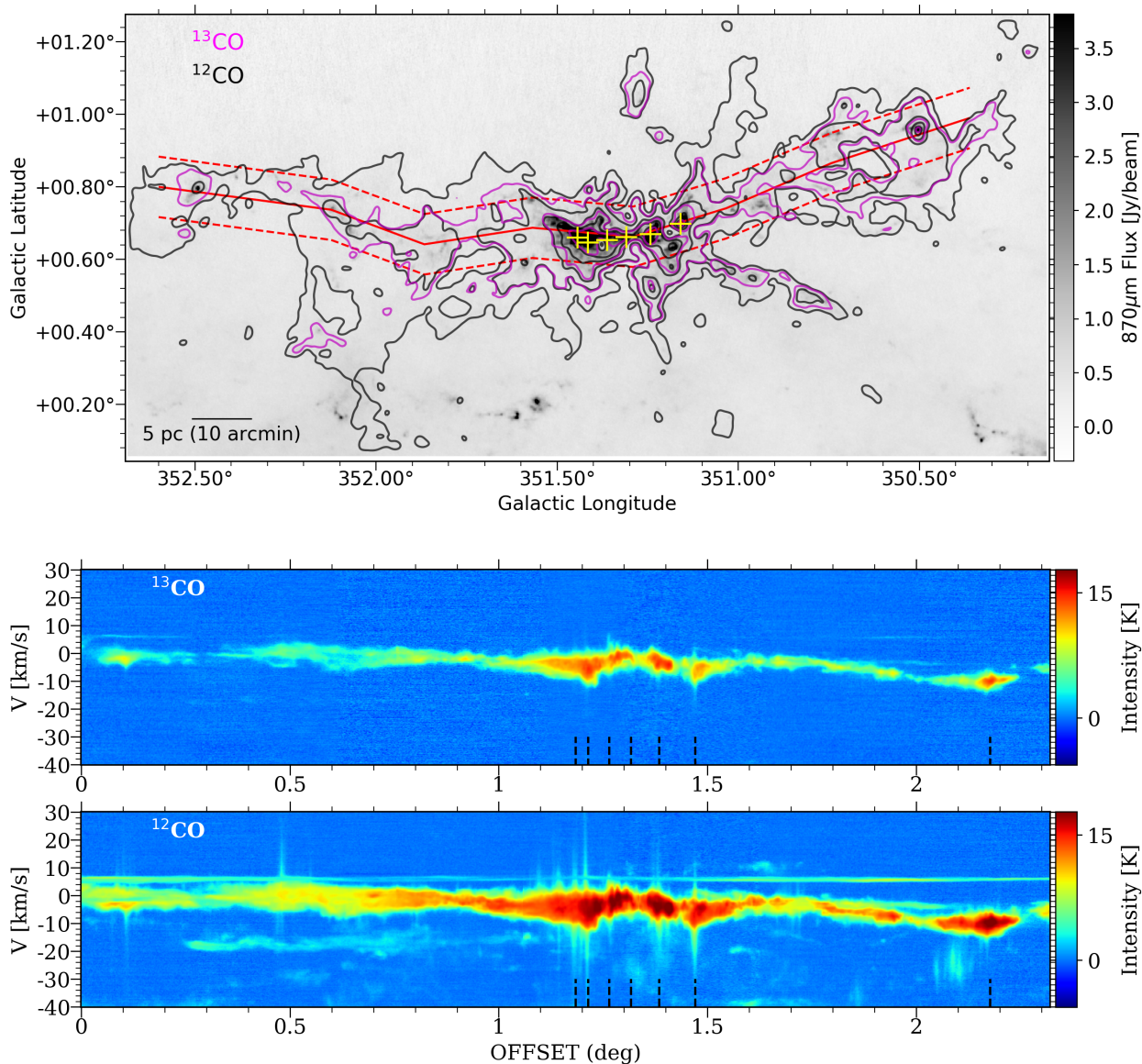


Fig. 5: Top: ^{13}CO (red) and ^{12}CO (black) emission contours overlaid on the $870\mu\text{m}$ ATLASGAL dust emission (gray scale). Contour levels are the same as in Figure 4. Middle and Bottom: Position-velocity maps of ^{13}CO and ^{12}CO , respectively. The dotted red lines on the top image show the path along which the PV maps are constructed. The offsets are the projected path length along the galactic longitude from east to west along the strip. On the PV-maps, projected offset positions of the far-infrared (FIR) sources (I[N], I to V from right to left) in the central filament and GM-24 region are indicated by dotted black markers at the bottom.

very bright and exhibits multiple bright emission spots. In areas that connect the central filament to the GM-24 region, ^{13}CO emission shows elongated and finger-like filamentary structures originating from the filament WF and spreading towards the south-west and north-west⁵. These features merge and reveal wide-spread emission in ^{12}CO (see bottom panel). Some elongated finger-like (pillar-like) emission structures going northward and south-ward from the central filament are prominently seen in both lines. In the eastern region, however, ^{13}CO emission is tracing only the trunk of the extended filament while ^{12}CO exhibits a more extended emission morphology that connects NGC 6334 with the star forming region NGC 6357 ($l=353.166^\circ$, $b=0.89^\circ$, see Fig. 1 in [Russeil et al. 2017](#)).

⁵ This study employs the Galactic coordinate system. We use ‘east’ (‘west’) to mean directions of higher (lower) Galactic longitude, while ‘north’ (‘south’) mean higher (lower) latitude.

Most of the bright emission spots in the central filament correspond to the far-infrared (FIR) sources shown by the yellow markers in Figure 4 (top panel). Numerous ATLASGAL $870\mu\text{m}$ dust emission clumps are located in this region. One interesting feature of the emission north of the central filament is that the gas emission seem to exhibit a pinched morphology. We over-plotted the position of the OB type stars from [Persi & Tapia \(2008\)](#) on the moment0 map of ^{12}CO . A circle of radius 8 pc (0.25 deg at 1.7 kpc) centered on the dominant O6.5 star is drawn in the map to match the arc-like emission morphology observed toward the NGC6334 central filament and it seems to perfectly match the morphological shape of the emission toward the north indicating that the high-mass star is likely interacting with the gas in the central ridge. However we also note that there are other OB stars, radio sources and H II bubbles located in the north to the

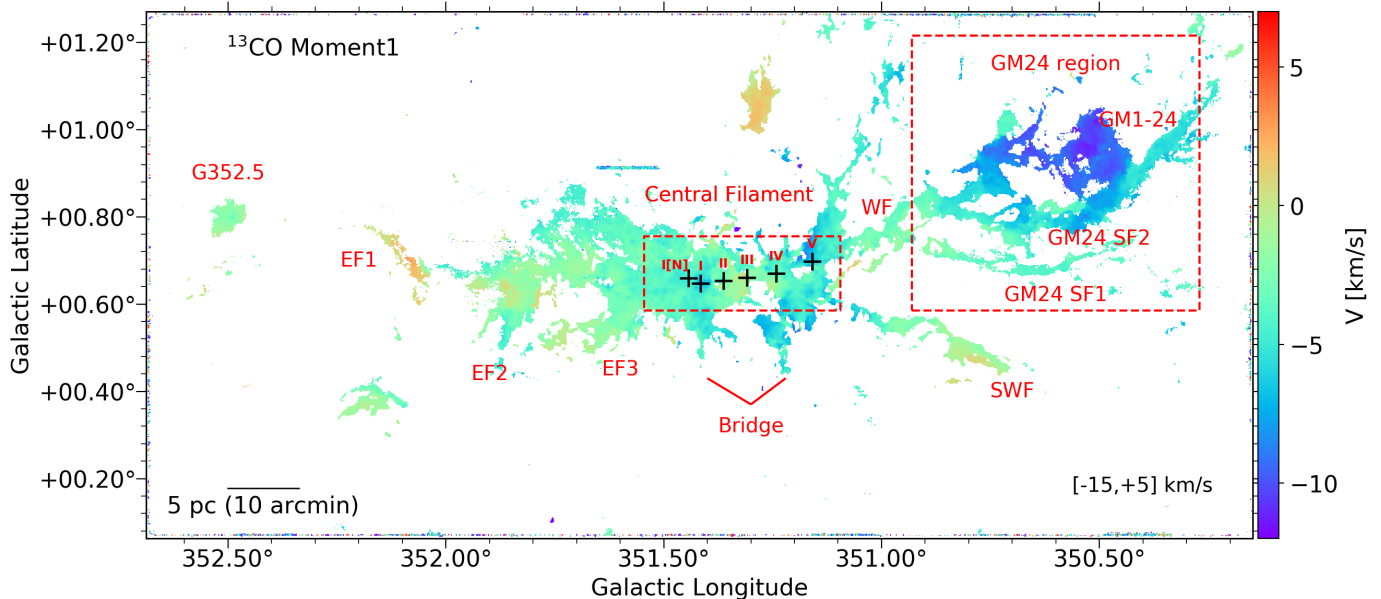


Fig. 6: Intensity weighted velocity map (moment 1) of the ^{13}CO emission toward the NGC 6334 extended filament. Labels are the same as in Figure 4

ridge (see Figure 1) that could have contributed in shaping the emission morphology of the central ridge.

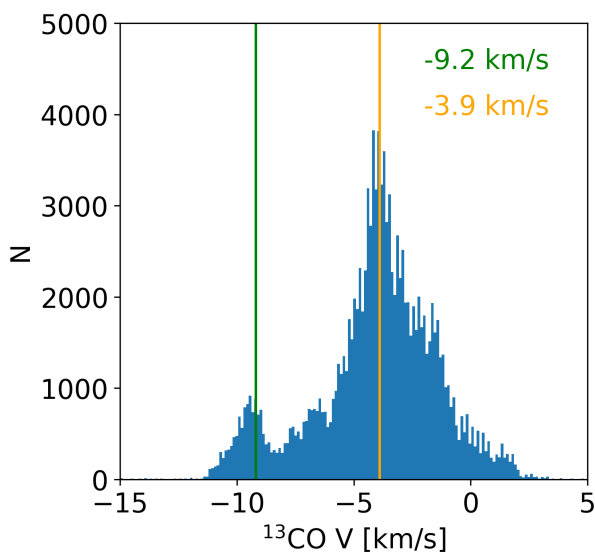


Fig. 7: Histogram of the ^{13}CO velocities obtained from the moment 1 map.

3.2. Gas velocity structure

3.2.1. Position-Velocity map

The middle and lower panels of figure 5 presents the Position-Velocity (PV) maps constructed for the emission within stripe defined by the three red lines in the intensity map (top panel).

The longitudinal extent of the PV maps is ~ 2.32 degrees. We find a ~ 80 pc long filament with a well connected and coherent velocity structure that has an average velocity of ~ -4.0 km s^{-1} .

Since the ^{13}CO line is mostly optically thin, it is tracing the higher column density gas regions along the NGC 6334 extended filament. High-velocity emission is not observed in ^{13}CO . In the ^{12}CO lines, since it is optically thicker, more diffuse extended emission features at intermediate to high velocities are visible that are not detected in ^{13}CO . Most of the high-velocity emission is observed mainly from the FIR source along the central filament and GM-24 (indicated by the dashed black markers in Figure 5). This high-velocity emission is most likely tracing outflows since it shows a clear correspondence with (high-mass) star-forming FIR clumps/cores embedded in the central ridge.

Gas emission at velocities of $\sim [-25, -15]$ km s^{-1} is observed at offsets from 0.3 to 1.3 deg. This emission is diffuse and exhibits no clear peaks in the PV map. The origin of this component is at present unknown. In lower excitation lines of CO, this velocity component is seen connected with the main filament (CO $J = 2 \rightarrow 1$, $1 \rightarrow 0$ in Fukui et al. 2018b, and $J = 2 \rightarrow 1$ in Arzoumanian et al. 2022).

Figure B.1 presents PV maps toward two selected slices averaged along the perpendicular direction to the central filament. The slices L1 and L2 indicate same regions as MFS-cold and MFS-warm presented in Arzoumanian et al. 2022 (see Fig. 12 in the paper). We observe V-shaped (or inverted) velocity structure along the L1 and L2 slices in higher J transitions of ^{13}CO . In addition, we also present PV-maps (Fig. B.1) toward six FIR sources in the central NGC 6334 ridge. Toward all the sources we observe similar V-shapes in the PV maps along the y-axis. While in FIR source I and II, V-shape appears in both velocity direction, FIR sources III and IV exhibit inverted V-shapes. Arzoumanian et al. 2022 interpreted these V-shaped emission features in PV maps as matter flowing within a sheet-like structure compressed by a propagating shock front. We further investigate the velocity structure around H II regions in Sec. 4.1.2 whether shock compression due to H II regions show similar velocity features in the molecular shells/rings around them.

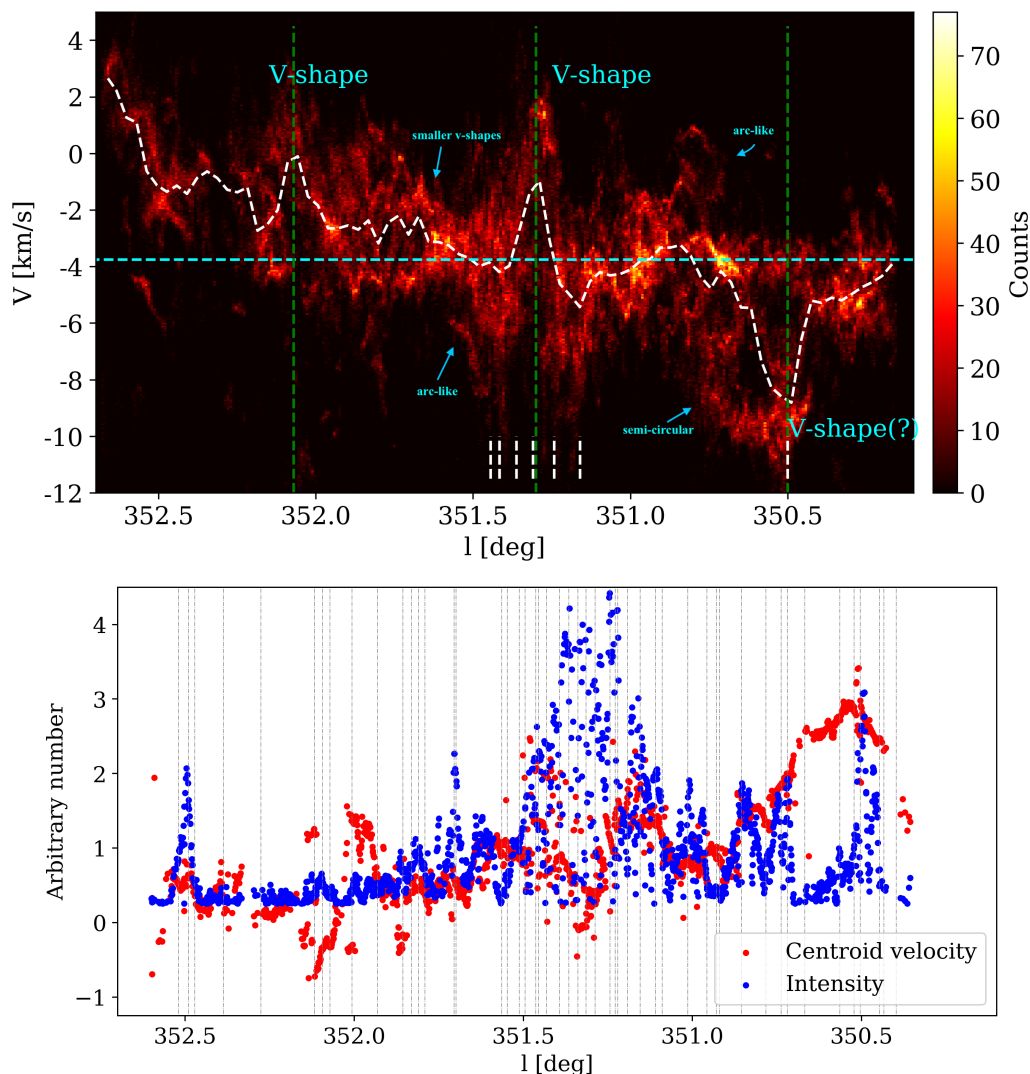


Fig. 8: Top : 2D histogram plot of ^{13}CO velocity components in the full observed region projected along the longitudinal direction from east to west. The bin sizes are 300×300 . The color bar shows the counts/density. The dotted white line follows the median velocities at a given longitude. The longitude of the six FIR sources I[N], I, II, III, IV and V, and also the GM24 region is indicated by the vertical dotted white markers. Also shown are the positions of the V-shaped velocity gradients (labelled in cyan color). Bottom: Velocity and intensity variation along the longitude within the PV-sliced region in Figure 5. The values in the y-axis are arbitrary numbers normalized by the mean values. The vertical black dotted lines indicate the longitudinal positions of the ATLASGAL clumps in the same region.

3.2.2. Intensity weighted velocity map

Figure 6 presents the moment 1 map of the ^{13}CO emission. We used a 7σ cutoff in integrated intensity to make the map. The velocity of the gas in the NGC 6334 extended filament shows primarily two components, one at -3.9 km s^{-1} and another component at -9.2 km s^{-1} . Figure 7 clearly illustrates double peaked distribution at these velocities. The -3.9 km s^{-1} velocity component reveals the coherent velocity structure of the extended filament while the -9.2 km s^{-1} velocity component is mainly tracing gas around the GM-24 region. However, it also appears to be tracing the ‘bridge’ structures. We see these features extending south from the FIR source I[N] and I and north-south from the central filament (from FIR sources IV and V, see Fig. 4). Widespread morphological existence of these two velocity components indicates that the molecular gas in NGC 6334 has at least two origins.

We also observe signs of velocity gradients in different regions. In the central filament, two ‘bridge’ features are at bluer velocities compared to the trunk of the central ridge. In the central ridge itself, we observe west to east velocity gradient with velocities becoming redder toward the east. Regions EF1, EF2 as well as the SWF filament also show signs of velocity gradients along the filament. A velocity gradient toward the central FIR sources III from both east and west of the central filamentary ridge is seen, which has also been reported by Zernickel et al. (2013) $\text{HCO}^+ J = 3 \rightarrow 2$ line data and interpreted as a sign of global collapse.

3.2.3. Multi Gaussian fitting to the ^{13}CO line cube

Given the complex velocity structure of the region, we also fit the ^{13}CO line cube using the Gausspyplus package (Riener et al. 2019). Gausspyplus is an automated fitting routine de-

veloped and tested to fit complex spectral profiles with a high degree of accuracy that was used in the analysis of the Galactic Ring Survey (GRS) (Jackson et al. 2006) (see Riener et al. 2019 for more detail). In this routine the spatial coherence is taken into account while fitting multiple Gaussian components. We applied a signal-to-noise ratio (S/N) of 3.0 to constrain the minimum value of ^{13}CO peak intensity. Figure A.2 presents the number of Gaussian components fitted to the ^{13}CO spectra within the NGC 6334 extended region. We find that to fit profiles of the brighter CO emission lines arising from the denser regions along the filaments require multiple Gaussian components to fit the line profiles.

Figure 8 (top panel) presents the resulting projected line of sight velocity components along the filament going from east to west in longitudinal direction (from now on called lv -plots). The velocities within the PV-sliced region shown in Figure 5 is presented in the bottom panel. The median velocities for each longitude bin are also shown in dashed white contours. In general, the projected velocities decrease from the east of the mapped region to the western direction. Gas velocities in the east of the extended NGC 6334 region are redder (0 to 4 km s $^{-1}$) while in the western region (near GM24) gas at bluer velocities (−3 to −12 km s $^{-1}$) are found. The velocity gradient over the full filament length (~ 80 pc) is much smaller than 1 km/s/pc, which also illustrates the velocity coherence of the filament.

Various features can be identified in the lv -plots, for example, smaller V-shapes, arch-like and semi-arch like shapes and semi-circular shapes highlighting the complex gas velocity structure in the region. Many of these features are possibly related to the feedback from the large number of H II regions located in the region. Indeed, complex velocity features around the H II regions are seen in lv and bv plots which will be discussed more in Section 4.1.2. We emphasize here that the amount of details of the velocity information one can see in the lv -plot, in which velocities are obtained from multi Gaussian fit to the spectra, is superior to the commonly used pv-diagram (see Figure 9).

The intensity and velocity along the dense ridge of the NGC 6334 extended filament show fluctuations or so called ‘wiggles’ at smaller spatial scales and also some broader V-shaped features (see Fig. 8, bottom panel). Similar oscillatory velocity fluctuations are also observed toward other Galactic filaments, for example, in $^{13}\text{CO}(1\rightarrow 0)$ observations toward the California nebula molecular filament (Guo et al. 2021).

Three broad V-shapes (or inverted V-shapes) in the lv -plot are indicated by the vertical dotted green lines in the figure at longitudes 352.1, 351.3 and 350.5 degrees. The base length of these V-shapes are broader than 3 pc. The V-shape around $l = 352.1^\circ$ is located in the eastern filament (EF1). Two others correspond to the central filament (toward FIR source III) and GM-24 region, respectively. In the GM-24 region, a closer look to the map shows that the velocity structure is rather complex and V-shape is only appearing in median velocity contour. Toward eastern filament (EF1) and central filament, we also observe similar V-shape in intensity variation but phase shifted with respect to the velocity structure. Typically the V-shapes in position velocity diagrams indicate gas compression (due to collision or due to H I/H II bubbles) (e.g., Inoue & Fukui 2013; Arzoumanian et al. 2022) or a global infall/collapse if observed with phase shifted intensity and velocity gradients (e.g., Hacar & Tafalla 2011; Zhou et al. 2023). We will discuss these features in Section 5.2 in conjunction with the observed CO emission morphologies in the channel maps.

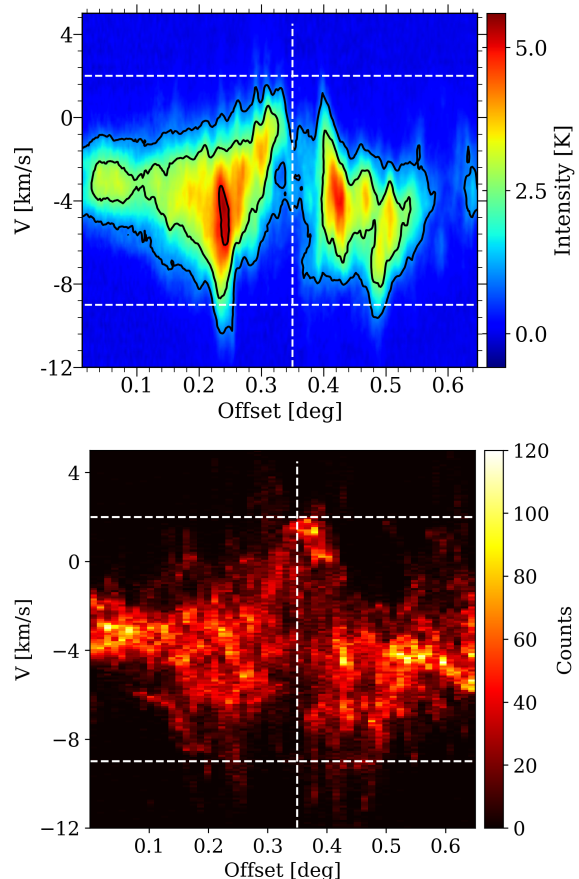


Fig. 9: PV-map (top panel) and lv -map (bottom panel) toward the NGC 6334 central region (path along $l = 351.0^\circ$ to 351.65° at $b = 0.67^\circ$). The PV-map uses intensity weighting for estimating the velocities while the lv -map is made using Gaussian velocity components of ^{13}CO spectra.

3.3. Channel maps

Figure 10 and 11 present channel maps of ^{13}CO and ^{12}CO in the velocity range -15 to $+5$ km s $^{-1}$, respectively, with steps of 2 km s $^{-1}$. The dotted circles in magenta indicate the H II regions and corresponding bubbles from Anderson et al. (2014). In addition, we have drawn three vertical dotted lines in black at longitudes 352.1° , 351.3° and 350.5° in different sub-plots. These are the positions of V-shapes features observed in the longitude-velocity plot of Figure 8. Text labels for various emission features (same as in Fig. 4) are also indicated in the channel maps. Also presented in Figures C.1 to C.3 are the zoomed velocity channel maps toward the central filament, GM-24 region and G352 region.

The channel maps allow a more detailed, velocity resolved view of the gas emission morphology. For example, at velocities -10 to -5 km s $^{-1}$ in both CO lines, the Eastern (near I(N) and I) and Western (near IV and V) parts of the NGC 6334 central filament show bright emission with no connecting ridge structure indicating that from -10 to -5 km s $^{-1}$, the two sides are disconnected. Note that these velocities are blue-shifted with respect to the average filament velocity of -3.9 km s $^{-1}$. From -5 , $+3$ km s $^{-1}$, we start seeing emission features connecting the two sides of the central filament. Only at velocities between -3 and $+1$ km s $^{-1}$, the connecting ridge is bright in both CO lines. One notable feature is that at these velocities and beyond on the redder side

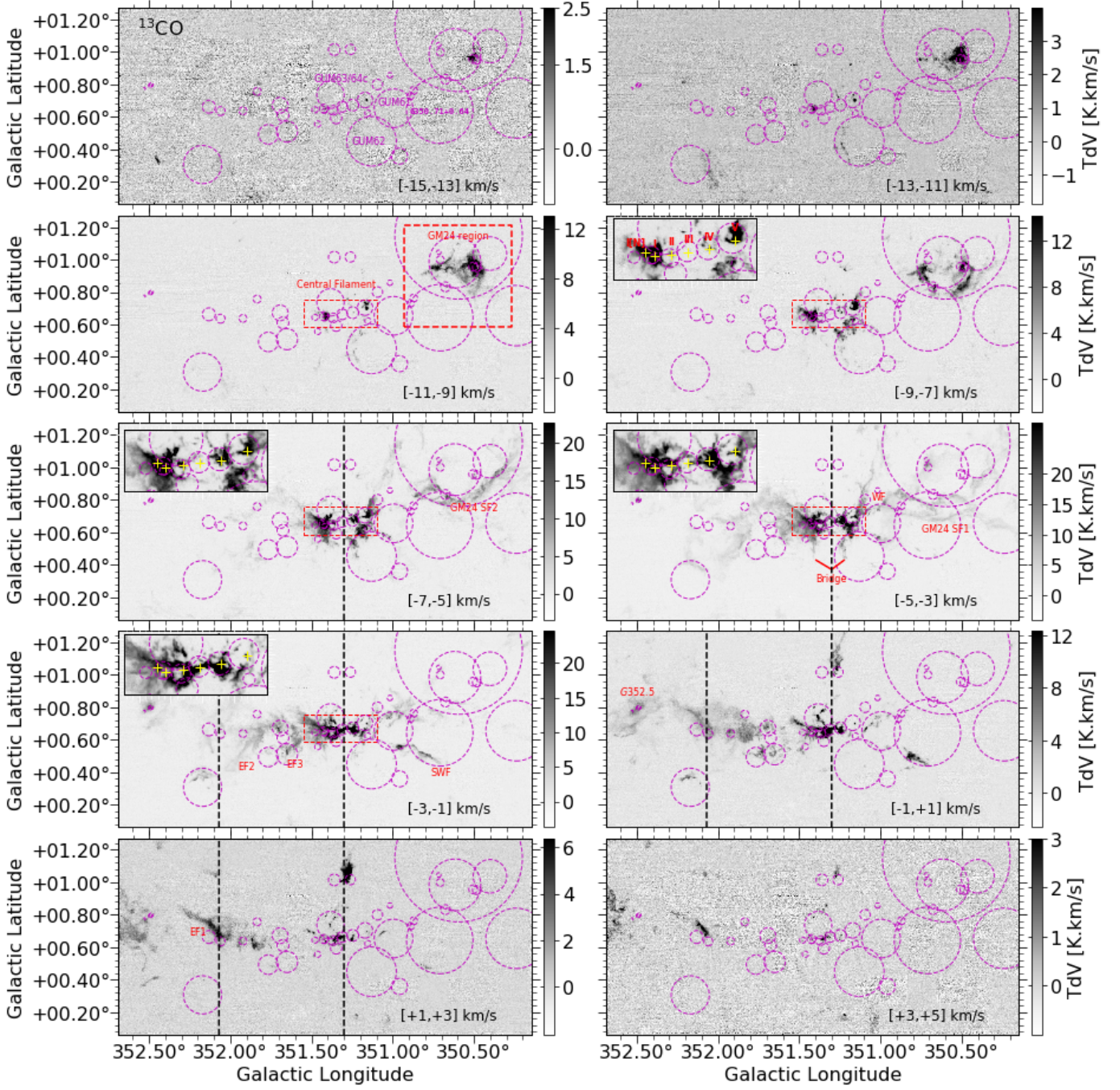


Fig. 10: Channel maps of ^{13}CO emission in the velocity range -15 to $+5$ km s^{-1} with steps of 2 km s^{-1} . Magenta dashed circles indicate H II bubbles from Anderson et al. (2014). Vertical black lines indicate positions of the broad V-shapes observed in $l\nu$ -plot in Figure 8. Labels indicating various emission features in the maps are same as in Fig. 4. Some optical H II regions (same as in Fig. 1) discussed in the text are also labelled in the top left channel map for a reference. For a clearer view of the channel maps, zoomed maps toward the central filament, GM-24 and G352 are presented in Fig. C.1 to C.3.

of the emission, the bright emission feature from FIR source V located in the Western part of the central filament is no longer visible.

Two parallel emission features, that we named the ‘bridges’ in the moment0 map in Figure 6, extend south from the central ridge at velocities -15 to -3 km s^{-1} in ^{13}CO . Both features are clearly visible and appear more extended in ^{12}CO . Toward these bridge features, we observe CO emission in both the -3.9 and -9.2 km s^{-1} velocity components (see Figure 7). The spatial co-

existence of the two gas components hints at a possible collision or a merger of the clouds in the central filament. The Eastern bridge extends south from FIR-sources I[N] and I, and is more apparent in velocities from -9 to -3 km s^{-1} . The western bridge extends south from FIR sources IV and V and is also visible at redder velocities up to -1 km s^{-1} in ^{12}CO . The latter emission feature also extends northward from source V up to latitude of ~ 1 deg toward the North-West.

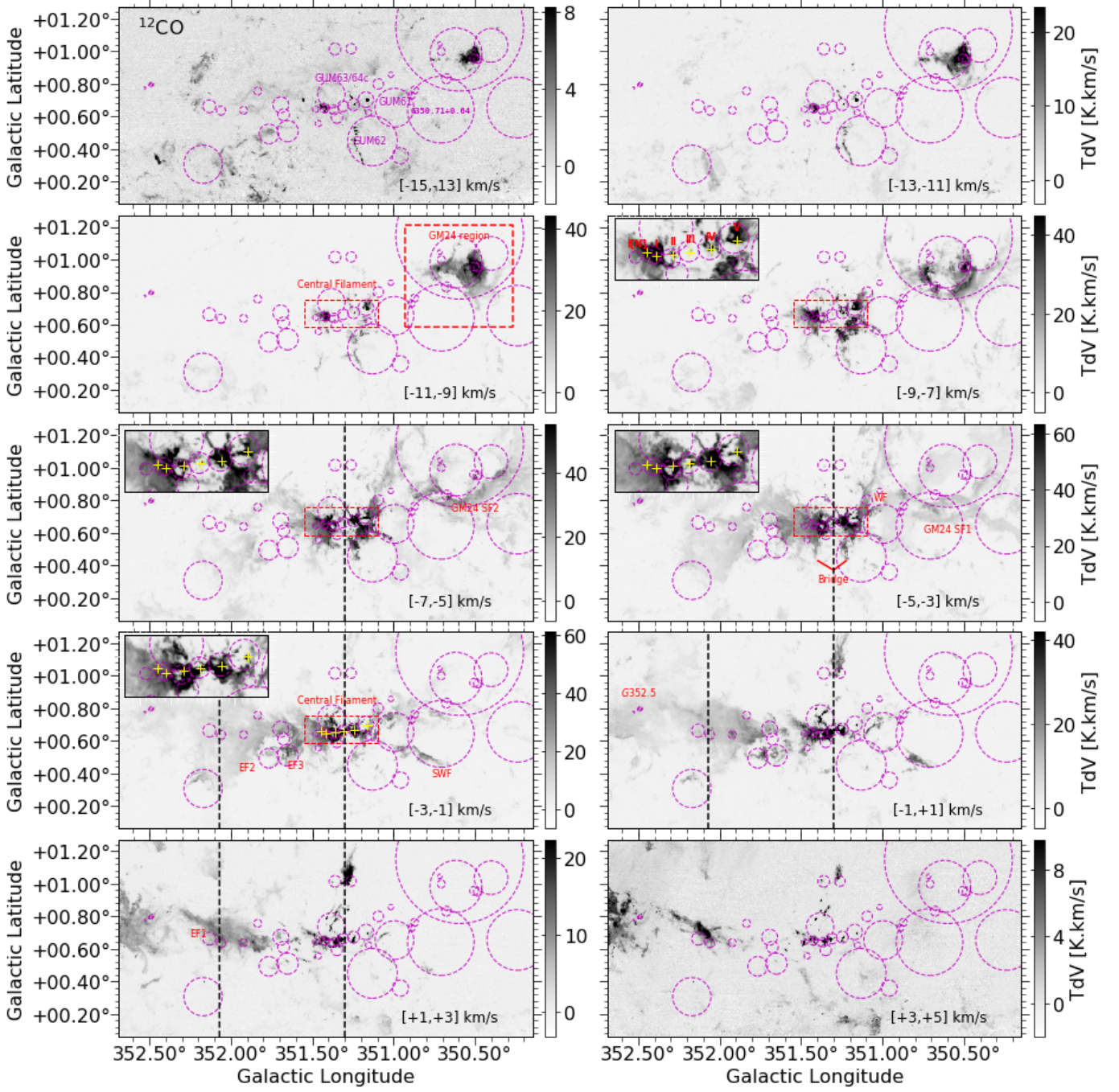


Fig. 11: Same as in Fig. 10 for ^{12}CO emission.

The GM24 region presents a clear example of bubbles within bubbles (see Fig. 1). In the channel maps this region is mostly bright in the -13 to -7 km s^{-1} velocity range. The connecting filaments (WF, SWF, SF1, SF2) located to the west of the central filament however are visible at velocities -7 to -1 km s^{-1} .

Regions located east of the central filament (EF1, EF2, EF3 and G352.5) are seen at velocities larger than -5 km s^{-1} . The ^{13}CO emission at this side of the filament is noticeably weaker. A bright elongated filamentary feature at around $l = 352.0$ deg, $b = 0.7$ deg is observed both in ^{13}CO and ^{12}CO at the velocities from -1 to $+5$ km s^{-1} . Emission at these velocities are also bright further east close to the NGC 6357 region at $l = 352.5$ deg and $b = 0.8$ deg. Finally to the South of the central filament (< 0.25

deg), there is little or no emission in velocities in between -15 and $+5$ km s^{-1} .

4. Analysis

4.1. Impact of H II regions in shaping the molecular gas structure

To study the impact of H II regions on the surrounding molecular gas and its velocity structure, we first visually inspect the gas emission morphology toward the H II regions located in the extended NGC 6334 region (see Fig. 1). For most of the H II regions a molecular emission counterpart is detected. Average ^{13}CO velocities of the molecular gas toward the H II regions are

presented in Table 1. The velocities are obtained using aperture extraction from the Gaussian fit velocities of ^{13}CO using radii of the H II regions. We observe a variety of emission morphologies around the H II regions such as bubbles exhibiting ring-like, arc-like shapes and/or central holes in the channel maps. Figure D.1 and D.2 show maps of ^{13}CO emission towards H II regions.

In the NGC 6334 central filament, eight H II regions are located along the ridge, most of which are associated with FIR sources (see Fig. 10 and 11). Channel maps only towards the central region are also presented in Figure C.1. H II region G351.348+0.593 is found in the South of the main ridge and G351.383+0.737 (GUM63/64) North to the ridge above sources I[N] and I. The central part of the ridge is disconnected up to bluer velocities of -5 km s^{-1} and exhibits connected filament only at redder velocities of -5 km s^{-1} (see Figure 10). Note that our identification of a broad V-shape in the $l\nu$ -plot is associated with this region (see Figure 9). We also find pillar-like structures above FIR source II (associated with GUM63/64C) and toward IV, observable both in ^{13}CO and ^{12}CO (see Figure C.1). Such pillars are identified in many PDR and H II regions, and thought to originate from the expansion of H II regions into a turbulent, non homogeneous medium (e.g., Tremblin et al. 2013).

To the west of the central filament, two optical H II regions, G350.995+0.654 (GUM61) and G351.130+0.449 (GUM62) are located south of the FIR sources IV and V. These regions are indicated and labelled in some panels in Fig. 10. In both CO channel maps in Fig. 10 and 11, we observe gas emission mostly at their edges but no emission is seen in the center indicating that these H II bubbles have already cleared out the gas around them and are at evolved stages. At velocities -1 to $+3 \text{ km s}^{-1}$, the emission at the southern edge of H II region G350.710+00.641 is bright in both ^{13}CO and ^{12}CO . In the velocity integrated intensity (mom0) maps (Fig. 4), this emission clearly appears filamentary, extending from source V to the South-West as a structure we named South-West Filament (SWF). These observations illustrate that H II shells could indeed play an important role in forming and shaping the morphology of filamentary cloud structures.

At the intersection of the H II regions G350.710+0.641 and G350.995+0.654 (GUM61), two smaller H II regions (G350.871+0.763 and G350.889+0.728) are seen. This is the region in which GM-24 southern filament 1 (GM24 SF1) departs westward from the West filament (WF). The filamentary emissions are clearly seen at velocities -5 to -1 km s^{-1} in the channel maps (Fig. 10 and 11).

The GM24 region is a clear case of bubbles within bubbles toward which we observe evidence of bubbles/shells interacting with gas around them and shaping the emission structure in the region. One example of such an interaction is seen where we observe two arc-like gas layers, one facing South and the other to the North at velocities -13 to -11 km s^{-1} surrounding the central bright emission spot in GUM1-24 (Figure 10 and 11, see zoomed maps of this region in Fig. C.2). These arch-like features correspond well with the shells of the H II regions G350.710+00.641 and G350.675+00.832 in the South and G350.401+01.037 in the North. At velocities between -9 and -7 km s^{-1} , we observe gas emission in a shell structure centered slightly east to GUM1-24. This shell structure corresponds to the H II region G351.130+0.449, located east to the compact radio source G350.50+0.95 (Russeil et al. 2016). In addition, we also find this shell-like gas emission structure confined within the radius drawn for H II bubble G350.594+1.149. Two HII regions G350.710+0.641 and G350.240+0.654 also appear to act on the the gas from the South in GM-24 region.

We see spiral/arch-like filamentary gas emission at velocities -7 to -3 km s^{-1} , that is associated with the GM24-SF1 and GM24-SF2 filaments (see also zoomed maps in Fig. C.2), connecting to the Western Filament (WF) and extending from south of the GM-24. At velocities -5 to -3 km s^{-1} , these filaments are more clearly visible in the channel maps (Figure 10 and 11), more so in ^{12}CO than in ^{13}CO emission. In fact, these emission features seem to intersect at the far west at $(l, b) = (350.4 \text{ deg}, 0.8 \text{ deg})$. We note here that these velocity ranges are slightly bluer but similar to the velocity of the main filamentary structure in the NGC 6334 region. Based on the observed gas distribution of these filaments in the channel maps we suggest that the gas structure is shaped by the group H II regions (G350.594+01.149, G350.617+00.984, G350.710+00.641, G350.995+00.654) (see Fig. 10, 11 and zoomed maps in Fig. C.2).

East of the central filament, at around $l = 351.5 \text{ deg}$ and at a similar latitude of the central filament, we find multiple H II regions. In particular four H II regions (G351.651+0.510, G351.676+0.610, G351.693+0.671, G351.766+0.492) appear to be connected to the gas at velocities -9 to $+1 \text{ km s}^{-1}$ (Figure 10 and 11). The emission of ^{13}CO at this side of the filament is noticeably weaker. A bright elongated filamentary feature at around $l = 352.0 \text{ deg}$, $b = 0.7 \text{ deg}$ is observed both in ^{13}CO and ^{12}CO at velocities of -1 to $+5 \text{ km s}^{-1}$. This is the same region (EF1) toward which we also observe the inverted V-shape in the $l\nu$ -plot (see Figure 8), the peak of which is at a longitude of $\sim 352.1 \text{ deg}$. Zoomed channel maps toward this region are presented in Figure C.3.

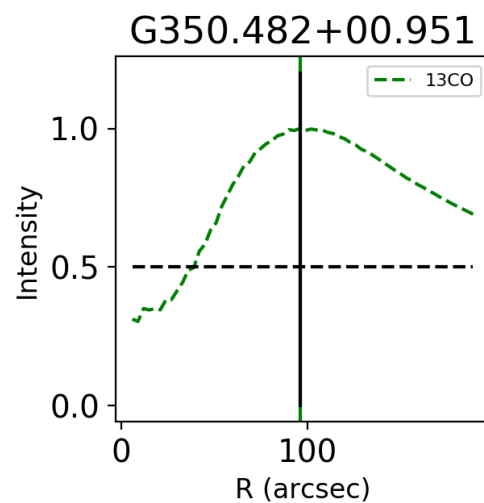


Fig. 12: Azimuthally averaged ^{13}CO radial intensity profile for the H II region G350.482+0.951 for the velocity range $[-15, +5] \text{ km s}^{-1}$. The intensities are normalized by the peak value. Vertical black line indicate the radius of the H II region from Anderson et al. (2014).

4.1.1. Radial profile and contrast parameter

To perform an unbiased search for shell/ring-like molecular structures around the H II regions, we plotted the azimuthally averaged radial ^{13}CO intensity profile of the H II regions (using a velocity range of -15 to $+5 \text{ km s}^{-1}$). For this we adopt the position and radius of the H II regions from Anderson et al. (2014) (cols. 3, 4 and 5 in Table 1) and plot the ^{13}CO intensity profile up to twice these radii. The positions and radii were obtained by

encircling the WISE mid infrared emission of the H II regions (see Anderson et al. 2014 for more details). In Figure 12, we present, as an example, the radial intensity profile toward H II region G350.482+0.951 associated with GUM1-24. This region exhibits a clear signature of a shell/ring like structure. In Figures E.1 and E.3, we present profiles of the ^{13}CO emission toward all the H II regions located in NGC 6334 extended region. We individually inspect the emission morphology toward the regions (Fig. D.1 and D.2) to interpret the radial profiles. We find two general categories of the intensity profiles plotted for full velocity range of -15 to $+5$ km s^{-1} .

The first category includes H II regions (22 of 42) that exhibit little emission or a flat emission profile toward their central regions and an increasing intensity profile outwards with respect to the H II radii. Some of these sources clearly exhibit a bumpy emission feature at corresponding H II radii (e.g., G350.482+0.951). In Figures E.1 and E.2, radial profiles of these H II regions are presented. The second category of the H II regions (15 of 42) exhibits centrally peaked emission within the adopted H II radii and a decreasing intensity profile outwards. A few H II regions (5 of 42) do not fall into either of these categories and exhibit flat profiles up to twice the adopted radii and only exhibit diffuse ^{13}CO emission. Intensity profiles of these H II regions are presented in Fig. E.3.

H II regions with little or flat profile emission toward the center and an increasing intensity profile outwards suggest that they are likely at later evolutionary stages since they appear to have cleared out the molecular gas from the center. More than half of the H II regions (14/22) with an increasing intensity profile exhibit a bumpy feature or an intensity maximum at/near their radii (Fig. E.1 and E.2), indicating a molecular shell/ring structure.

On the other hand, centrally peaked ^{13}CO emission toward H II regions likely reflects an early evolutionary stages. However, it is also possible that these sources have line of sight contamination that caused their profiles appear centrally peaked. To investigate this we explore the ^{13}CO line profiles for emission averaged over different velocity ranges within -15 and $+5$ km s^{-1} with a step of 5 km s^{-1} . Among the 20 H II regions that show either centrally peaked and decreasing or flat profiles for emission averaged over the full -15 to $+5$ km s^{-1} range, we find that the profiles of 14 of them either increase outward or show a bumpy feature when plotted for different velocity ranges. These profiles are also shown in Figure E.3. In total, we find 36 of 42 H II regions (86%) that show the signature of molecular gas having been cleared from their center and that exhibit an increasing intensity profile outward or a shell/ring-like molecular structure around them.

These characteristics of molecular line emission features are noted in col. 8 of Table 1. Centrally peaked and decreasing intensity profiles are annotated by ‘CP’, increasing profiles are annotated by the letter ‘I’, shell/ring-like structure are annotated by the letter ‘S’ and sources with flat profiles are annotated by an ‘F’. The four 5 km s^{-1} wide velocity ranges within -15 to $+5$ km s^{-1} for which these structures are found are also noted, with V1 to V4.

We also estimate sizes of the ^{13}CO emission associated with the H II regions from the ^{13}CO line profiles. For H II regions with clearly decreasing or increasing radial profiles we obtain the sizes at which the intensity is 50% of the peak emission (indicated by the vertical green lines in Figures E.1 to E.3). For H II regions exhibiting a shell/ring like morphology, we adopt the radii where these bumpy or shell-like features are observed. In column 6 of Table 1, the sizes estimated from molecular line emission associated with the H II regions are presented. In gen-

eral there is a tentative agreement between the sizes that we estimated from ^{13}CO emission profile and the sizes reported by Anderson et al. (2014). The mean and standard deviation of the difference in radius are $\sim 15\%$ and $\sim 40\%$ with respect to the radius from Anderson et al. (2014). The intensity profiles of H II regions with shell/ring like structure begins to increase at a certain inner radius, which varies from source to source (see Figure E.1). We find that the inner radii can have values as small as $\sim 40\%$ of the shell radii.

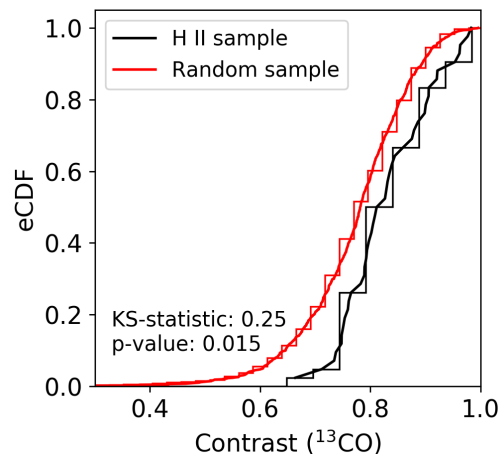


Fig. 13: Empirical cumulative distribution function (eCDF) of the contrast values measured for the H II regions (black) and 1000 randomly created rings (red) in the mapped region. The two sample ks-test results are also annotated.

We employ a contrast measurement method that quantifies the enhancement of the molecular line intensities at the H II region/bubble radii. To do so, we define a contrast parameter C as;

$$C = \frac{W_{R_2} - W_{R_1}}{W_{R_2}},$$

where, W_{R_1} and W_{R_2} give sum of the integrated molecular line intensities within the radii of sizes R_1 and R_2 , respectively. R_1 represents the size of the inner ring and R_2 represents the size of the outer ring. The significance of the parameter for a homogeneous medium is straightforward and proportional to the ratio of the area of the ring to the area of the outer radius considered.

Column 9 of Table 1 presents the ^{13}CO contrast parameter values for H II regions computed from the velocity range -15 to $+5$ km s^{-1} for radius ranges of 0.6 to 1.2 times the radius. For H II regions with shell-like intensity profiles, we find that the inner radii at which the intensity starts increasing is up to 40% of the shell radii. In addition, since H II regions/bubbles are known to be eccentric (Churchwell et al. 2007), these choices of radii between $0.6 R$ to $1.2 R$ to measure the contrast parameter incorporate the eccentric nature of the bubbles with eccentricity values of 0.86 to 1 . Contrast parameter values larger than the expected value of 0.75 for the radii considered here are presented in col. 9 of Table 1. At these velocity ranges and radii, 21 H II regions show higher contrast parameter than 0.75 . However, at segmented velocity ranges from -15 to $+5$ km s^{-1} with a step of 5 km s^{-1} , we already found that the majority of the H II regions show centrally clear or flat profiles that either increase outward or show a bumpy feature at or near the corresponding radii. Therefore, we measured the contrast parameter for velocity ranges from -15 to $+5$ km s^{-1} with a step of 5 km s^{-1} . The maximum value of the contrast parameter (C_{max}) in these velocity

Table 1: Molecular line emission characteristics of WISE H II regions in NGC 6334.

WISE H II source	Type	l ($^{\circ}$)	b ($^{\circ}$)	R ($''$)	R(^{13}CO) ($''$)	V(^{13}CO) km s $^{-1}$	† Emission profile	C	‡ C $_{max}$	§ N $_{clump}$
G350.240+00.654	C	350.240	0.655	670	498	-3.8	I,V2	—	0.78	1
G350.401+01.037	G	350.401	1.037	372	546	-8.3	I,S	0.95	0.96	5
G350.482+00.951	K	350.482	0.952	96	96	-9.6	I,S	0.81	0.88	1
G350.505+00.956	K	350.505	0.957	96	84	-10.0	I,V3	—	—	1
G350.594+01.149	G	350.594	1.149	1413	1314	-6.6	I,S	—	0.84	26
G350.617+00.984	G	350.617	0.984	574	474	-8.1	I,S	0.76	0.80	14
G350.675+00.832	G	350.675	0.832	108	156	-6.8	I,V3	—	0.79	1
G350.707+00.999	C	350.707	0.999	86	84	-5.0	I,S	0.76	0.89	1
G350.710+00.641	G	350.710	0.642	737	330	-4.2	I,S	0.85	0.98	21
G350.716+01.044	Q	350.716	1.045	50		-4.1	F	0.77	0.79	
G350.871+00.763	Q	350.871	0.763	86	36	-1.9	I	0.82	0.83	
G350.889+00.728	Q	350.889	0.729	76	96	-2.0	I,V2	—	0.83	1
G350.958+00.358	K	350.958	0.359	179	135		I,S	—	0.92	
G350.995+00.654	K	350.995	0.654	428	330	-3.3	I	0.90	0.92	22
G351.017+00.856	Q	351.017	0.857	59			I	0.80	0.80	
G351.094+00.800	Q	351.094	0.800	116		-4.5	I,V2	—	0.79	
G351.130+00.449	K	351.130	0.450	549	534	-5.1	I,S	0.95	0.96	8
G351.153+00.623	Q	351.153	0.623	68		-4.9	I	0.80	0.83	1
G351.170+00.704	K	351.170	0.704	171	300	-5.1	I,V3	—	—	3
G351.246+00.673	K	351.246	0.673	131	108	-3.3	CP	—	—	4
G351.261+01.016	K	351.261	1.016	114	111	1.4	I,S	0.81	0.81	1
G351.311+00.663	K	351.311	0.663	119	162	-2.0	I,V2	—	—	3
G351.348+00.593	G	351.348	0.593	125	54	-2.5	I,S	0.80	0.91	3
G351.360+01.015	K	351.360	1.015	129	66	1.3	I,V4	—	—	
G351.367+00.640	K	351.367	0.641	107	132	-2.9	I,S	0.83	0.95	4
G351.383+00.737	K	351.383	0.737	303	222	-3.6	I,S	0.81	0.98	14
G351.420+00.637	Q	351.420	0.638	52		-5.6	F	—	—	3
G351.424+00.650	G	351.424	0.651	99		-5.0	CP	—	—	4
G351.462+00.556	G	351.462	0.557	68	42	-3.6	I	0.84	0.88	
G351.479+00.643	Q	351.479	0.644	68		-4.2	F	—	0.76	2
G351.651+00.510	K	351.651	0.510	234	96	-1.7	I,V2	—	0.80	
G351.676+00.610	G	351.676	0.611	130	162	-2.4	I	0.89	0.90	
G351.693+00.671	K	351.693	0.672	175	180	-2.1	I,V2	—	0.79	
G351.766+00.492	G	351.766	0.493	217	318	-1.1	CP	—	0.91	
G351.835+00.756	Q	351.835	0.757	87		-0.2	I	0.76	0.84	
G351.922+00.638	Q	351.922	0.638	86	69	-0.3	I,S	—	0.86	1
G352.060+00.636	Q	352.060	0.636	99		1.0	F	0.76	0.76	
G352.132+00.663	C	352.132	0.663	143	72	0.8	I	0.80	0.81	
G352.171+00.307	C	352.171	0.307	423	378	-1.9	I,S	—	0.90	2
G352.486+00.799	C	352.486	0.799	43		-2.3	I,V4	—	0.83	
G352.493+00.793	C	352.493	0.794	40	42	-2.4	CP	—	—	
G352.529+00.775	Q	352.529	0.775	22		-1.7	I,V4	0.77	0.77	

Notes. Cols. 1 to 5 (H II region name, type, longitude, latitude and radius, respectively) are taken from [Anderson et al. 2014](#). The sizes of the molecular shells/rings (R(^{13}CO)), molecular line velocities (V(^{13}CO)) and contrast parameter values (C) are determined from this work. † ^{13}CO radial profiles. CP: centrally peaked, I: increasing profile, S: shell-like feature, F: flat profile. V1: $[-15,-10]$ km s $^{-1}$, V2: $[-10,-5]$ km s $^{-1}$, V3: $[-5,0]$ km s $^{-1}$, V4: $[0,+5]$ km s $^{-1}$. ‡ Maximum value of the contrast in one of the velocity ranges. § Number of ATLASGAL clumps (from [Urquhart et al. 2018a](#)) located at H II radii range 0.6R–1.2R.

ranges are given in Col. 10 of Table 1. In total, using the contrast measurement method we identify 34 of 42 H II regions (81%) that exhibit intensity enhancement of the molecular emission at the H II radii.

We performed a two sample ks-test between contrast parameters (C_{max}) measured for the H II regions and contrast parameters measured toward a randomly created 1000 shells/rings in the mapped region. Sizes of these randomly created rings range from 20" to 700", similar to the sizes of the H II regions. The ks-test statistics (0.25) and p-value (0.015) suggest that the sample of H II regions is indeed distinct from that representing the randomly created ring structures. Figure 13 presents the empirical cumulative distribution function (eCDF), which clearly shows that H II regions have a higher probability of get-

ting higher contrast values. Even though most H II regions in our sample show a contrast parameter above the expected value, it is wise to explore the significance of that parameter. To do so we exploited the contrast values derived for the randomly sampled shells/rings and fit a Gaussian distribution with mean and standard deviation of 0.78 and 0.09, respectively (Fig. E.4). Then we define a contrast threshold above 1σ from the mean, which is 0.87. 14 H II regions show contrast values above 1σ threshold in at least one velocity ranges (-15 to $+5$ with a step of 5 km s $^{-1}$) for a shell/ring radii of 0.6 to 1.2 times the H II radius. We repeated the analysis considering smaller shell/ring sizes (0.6R–1.0R and 0.8R–1.2R). In total, we find 22 H II regions (52%) show a contrast parameter above 1σ threshold in at least one radii and velocity ranges.

Caveats of using contrast method are that for the H II regions that are too young to have created a shell/ring like structure and are still embedded in their dense natal gas, or exhibit a complex morphology, e.g., shaped by a champagne flow, this method may not provide the meaningful results. In addition, both the radial profile and the contrast method applied in this study cannot distinguish the true morphological features if a shell has a full-ring, half-ring or has a clumpy edge. To study the morphology in detail, 2D or 3D emission maps (channel maps) have to be examined. For a larger shell/ring sizes, radii at which contrast is being measured should be carefully selected. Despite the caveats, the contrast method in conjunction with radial profiles can be a useful tool to study H II bubbles/regions, in particular to search for shell-like structures, using large scale Galactic molecular line and continuum surveys.

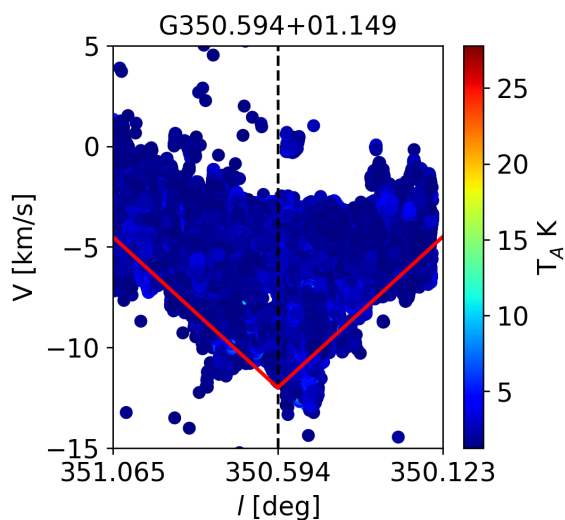


Fig. 14: lv plot toward H II region G350.594+1.149. Observed V-shaped emission structure is indicated by the red lines.

4.1.2. Longitude-velocity (lv) and latitude-velocity (bv) plots toward H II regions

In figures F.1 to F.5, we present longitude-velocity (lv) and latitude-velocity (bv) plots for the H II sources. For the plots, we used the Gauss fitted ^{13}CO velocities instead of the commonly used intensity averaged pv -plot. We again used the radii range of $\pm 1.2R$ in both longitudinal and latitudinal direction, where R is the H II region radius. To investigate if we observe higher intensities around the H II regions, we made the plots with intensity color wedges. Toward some H II regions (12/42) we find the velocity structure to have to follow a (partial) elliptical shape either in lv or bv plots. For those, we also present approximate expansion velocities inferred from visually fitted ellipses in Table F.1. We also observe broader V-shaped velocity feature, with open cavities or with filled emission. An example of the lv plot toward H II region G350.594+1.149 is shown in figure 14 in which the observed V-shaped emission structure is also indicated by the red lines. Toward 15 H II regions (in lv or bv plots), we observed such features (Fig. F.1 to F.5). In particular these features were observed toward the sources located in and around the filaments (see F.6). We interpret these velocity structures to represent shock compressed gas layers driven by H II regions in the filament or located nearby. To further investigate the features around these H II regions, we made pv maps along different

slices (L3 to L12) shown in F.6. These pv maps are constructed along perpendicular direction of the filament axis or the clumpy regions located at the edges of the H II regions. In all slices (except for L7 and L12) we observe V-shaped emission velocity feature. While in slices L7 and L12, we only observe a velocity gradient. Overall the lv and bv plots highlight complex velocity structure around H II regions and in particular their role in shaping the gas velocity structure around them. These results further illustrate multiple sites of gas compression due to H II regions in the extended NGC 6334 region.

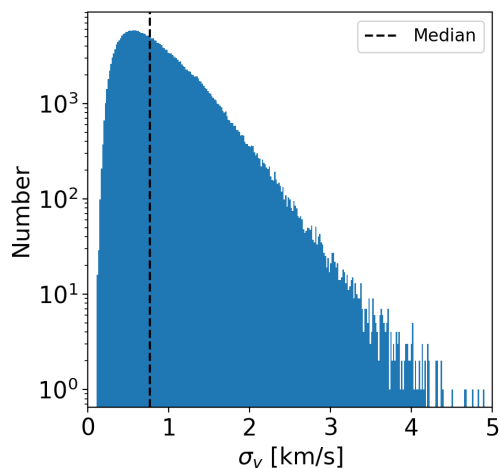


Fig. 15: Histogram of velocity dispersion (σ_v) values determined from the Gaussian fit to the ^{13}CO line profiles.

4.2. Velocity dispersion in NGC 6334 extended region

Figure 15 presents a histogram of the velocity dispersion (σ_v) determined from the Gaussian fit to the ^{13}CO line profiles toward the mapped region. Mean and median values of the distribution are 0.9 and 0.8 km s^{-1} , respectively. We then made maps for different velocity dispersion ranges $\sigma_v \geq 2$, $2.0 > \sigma_v \geq 0.9$ and $0.9 \leq \sigma_v < 0.9 \text{ km s}^{-1}$ (top to bottom panels in Figure 16). The gas with velocity dispersions lower than 0.9 km s^{-1} (mean value), represents the extended regions. At an increased dispersion level from 0.9 to 2 km s^{-1} , the emission mostly corresponds to the dense ridges along the filament while three regions (EF1, central ridge and GM24-SF2) exhibit velocity dispersions higher than 2 km s^{-1} . Except toward a few H II regions, we do not observe significantly higher velocity dispersions associated with the H II shells. This could mean that H II regions play a minor role in injecting turbulence to the large scale gas distribution. In the NGC 6334 extended region, we found that the velocity dispersion is well correlated with the dense gas structure along the filament. This indicates that the origin of the velocity dispersion is likely related to formation of the filaments themselves. The large values of dispersion toward the NGC 6334 central ridge and filament EF1, $\sigma_v \geq 2$, may reflect global collapse of gas onto the filaments. Both of these regions have a broad V-shape velocity structure in the lv -plot which will be discussed in Section 5.2.

5. Discussion

5.1. Velocity coherence and fluctuations

The NGC 6334 filamentary structure was studied in lower excitation lines of CO by Arzoumanian et al. (2022). Based on their

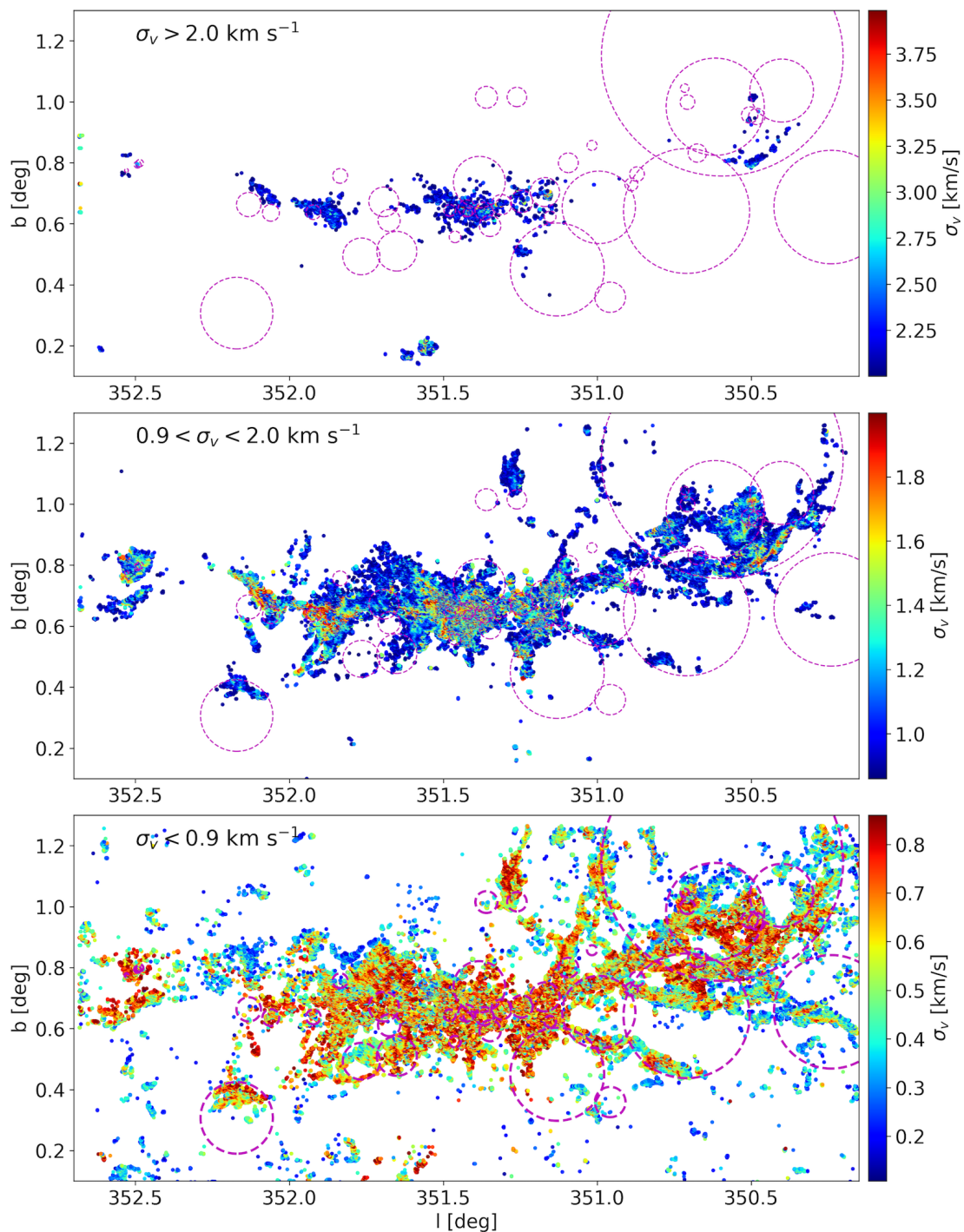


Fig. 16: Velocity dispersion measured from ^{13}CO Gaussian fit. Dispersion velocity ranges are presented on top left corner of each plot and also shown are the H II sources from the catalog of (Anderson et al. 2014).

position-velocity map, these authors reported a ~ 50 pc sized velocity coherent structure between $l = 350.4^\circ$ and 352.6°). In this study, with the higher resolution data and improved method for creating position velocity map by following the dense gas ridge along the filament, we investigated the velocity structure in the NGC 6334 extended region ($l = 350.15^\circ$ to 352.65°) (see Section 3.2). We found that the extent of the filament in which we observe the velocity coherent structure is ~ 80 pc in length and thus longer than previously thought. The velocity gradient along the entire filament (~ 80 pc) is much smaller than 1 km/s/pc

which quantitatively illustrates its velocity coherency. Such coherency in large scale structures is also found in the simulations of galactic filaments (e.g., Duarte-Cabral & Dobbs 2016; Smith et al. 2020). In a recent review of the filamentary ISM, Hacar et al. (2023) suggest that velocity coherency could simply be a necessary feature of survival of the large filaments since larger gradients would otherwise lead to their rapid destruction.

We also observed smaller scale velocity and intensity fluctuations (or so called ‘wiggles’) along the filament (see Section 3.2 and Figure 8). These fluctuations or oscillatory features in

the velocity centroid and intensity (with phase shift) are thought to trace core-forming flows or local density enhancement in the filament (e.g., [Hacar & Tafalla 2011](#); [Guo et al. 2021](#); [Henshaw et al. 2020](#)).

5.2. Multiple gas compression, global collapse and infall

We studied both localized and the large scale velocity structure of the NGC 6334 filament using position velocity diagrams (see Sect. 3.2). In addition to the commonly used position-velocity plots, which are intensity weighted, we used longitude/latitude velocity (lv or bv) plots using the Gauss fitted velocities from ^{13}CO line profiles. We investigated the velocity structure toward the FIR sources in the central filament and also toward the H II sources located in the extended region. Toward all the FIR sources we observe V-shaped (inverted V-shape) velocity structures latitude-velocity plots (see Fig. B.1). Toward the H II regions the lv and bv plots exhibited a variety of complex velocity features (see Fig. F.1 to F.5). A more common feature is again the V-shape (inverted V-shape) velocity structure particularly toward sources that are located in or adjacent to the filament. The V-shape velocity features are thought to trace gas compression due to propagating shock fronts or colliding flows (for example, [Inoue & Fukui 2013](#); [Fukui et al. 2018b](#); [Arzoumanian et al. 2022](#)). Formation of molecular clouds after multiple compressions in interacting shells or bubbles has been proposed in theoretical studies (e.g., [Inutsuka et al. 2015](#)). Our observations of multiple gas compression features observed toward H II shells/radii, as well as toward FIR sources in the central ridge support this scenario.

On a larger scale, we have identified broader V-shape velocity structures toward the NGC 6334 central filament, the GM-24 region and EF 1 (the G352 region) in the median velocity contours projected along longitude direction (see Figure 8 in Section 3.2). We discuss these three regions individually here.

5.2.1. NGC 6334 central filament:

The NGC 6334 central filament is approximately 10 pc long and runs almost parallel to the Galactic plane (see Figure 4). Three distinct properties of the gas velocity structure are observed toward this region.

First, the east and west side of the central ridge exhibit bright emission at blue-shifted velocities with respect to the average velocity of the NGC 6334 central filament -3.9 km s^{-1} . This is evident from the channel maps presented in Figure 10 and 11. The case for a global collapse scenario has already been made by [Zernickel et al. \(2013\)](#) for this filament. Our observations provide further evidence of the globally collapsing gas in the NGC 6334 central ridge.

Second, we observed a broad inverted V-shape structure in the lv -plot (see Figure 8). The base length of the V-shape is ~ 6 pc (0.2 deg at 1.7 kpc) and it is located between FIR sources II and IV. Additionally, we also observe the intensity fluctuation phase shifted with respect to the observed velocity structure (Figure 8, bottom panel). Such V-shapes indicate gas compression (due to collision or due to H I/H II bubbles) (e.g., [Inoue & Fukui 2013](#); [Arzoumanian et al. 2022](#)) or a global infall/collapse if observed with phase shifted intensity and velocity gradients (e.g., [Hacar & Tafalla 2011](#); [Zhou et al. 2023](#)). The velocity gradient inferred from the arms of the V-shape is $1.3 \text{ km s}^{-1} \text{ pc}^{-1}$. Assuming the observed velocity gradient is due to free fall and using the extension of V-shape ($R \sim 3$ pc), we estimate a kinetic

mass ($M \approx 2R^3 \nabla v^2 / G$; see Eqn. 1 in [Zhou et al. 2023](#)) of the central filament of $\sim 2 \times 10^4 M_{\odot}$. The mass estimate from the free fall assumption is consistent with the reports of line mass per unit length of $1000 M_{\odot} \text{ pc}^{-1}$ toward the central NGC 6334 filament by [André et al. \(2016\)](#).

Third, toward both longitudinal ends of the central filament, we observe two ‘bridge’ structures (see Figure 17). The gas emission in the bridges correspond to the bluer velocity component (-9.2 km s^{-1}) shown in Figure 7. From ^{12}CO and ^{13}CO emission properties, it is clear that these are prominent dense gas structures, filamentary in nature, and running almost perpendicular to the central ridge of the main filament. The same gas velocity component is also associated with GM-24 region. From the central ridge, the eastern bridge feature in ^{12}CO (3-2) emission extends approximately 7 pc to the south while the western bridge is about 15 pc long extending both toward south and north passing from FIR source V. The south extension of the west bridge from sources V is ~ 8 pc. Along the central ridge both the -3.9 km s^{-1} and the -9.2 km s^{-1} velocity components coexist spatially. This hints mixing of the gas either due to collision or merger of the clouds.

[Fukui et al. \(2018b\)](#) presented a cloud-cloud collision scenario in which the -20 km s^{-1} filamentary cloud is in collision with the NGC 6334 filament. In fact, we also observe at velocities $[-25, -15] \text{ km s}^{-1}$ a feature in ^{12}CO emission, but not in ^{13}CO . The emission morphology presented in Figure 18 at this velocity range runs north-east to the central filament (with reference to the source I[N]). This emission region extends from (351.5 deg, 0.8 deg) to (352.2 deg, 0.5 deg). We refer to this as the Northern Filament and have labeled it “NGC6334-NF” in the figure. This emission feature is also detected in CO (2-1) and CO (1-0) and is connected in the position velocity map with the central NGC 6334 filament (see [Fukui et al. 2018b](#); [Arzoumanian et al. 2022](#)). The detection of higher excitation $J = 3 - 2$ lines of CO in this work indeed indicates that it also contains relatively denser gas but likely at quiescent phase since no ATLAS-GAL clumps are detected toward this region. According to [Fukui et al. \(2018b\)](#), cloud-cloud collision scenario explains the observations of the “bridge” features. In addition they also postulate that the cloud collision is happening at different locations at different time scales and, therefore, giving rise to the different evolutionary phases of the NGC 6334 extended filament from west to east. GM-24 region located in the west is an evolved phase, the central ridge is in an active phase of star formation, and, the filament to the east (G352 region) is in a quiescent phase. We suggest that the spatial and kinematic connection of the NGC6334-NF filament and the ‘bridge’ features with the main gas velocity structure should be considered in explaining star formation in the NGC 6334 filamentary complex.

5.2.2. GM-24 region:

A broad inverted V-shape is observed toward the GM-24 region in the median velocity contour in the lv -plot (see Fig. 8). However, the GM-24 region contains gas emission at both -3.9 km s^{-1} and -9.2 km s^{-1} . Therefore the broad V-shape in median velocity contours shown in Figure 8 does not exactly illustrate the velocity structure. [Fukui et al. \(2018a\)](#) suggested cloud-cloud collision scenario toward this region based on the complimentary distribution of gas emission at two velocities (-10 and -6 km s^{-1}) and the V-shape observed in position velocity map of ^{12}CO 2-1 at spatial resolution of $90''$. Our LAsMA observations with $20''$ spatial resolution do not confirm complimentary distribution of the gas. We find that the observed gas emission morphology

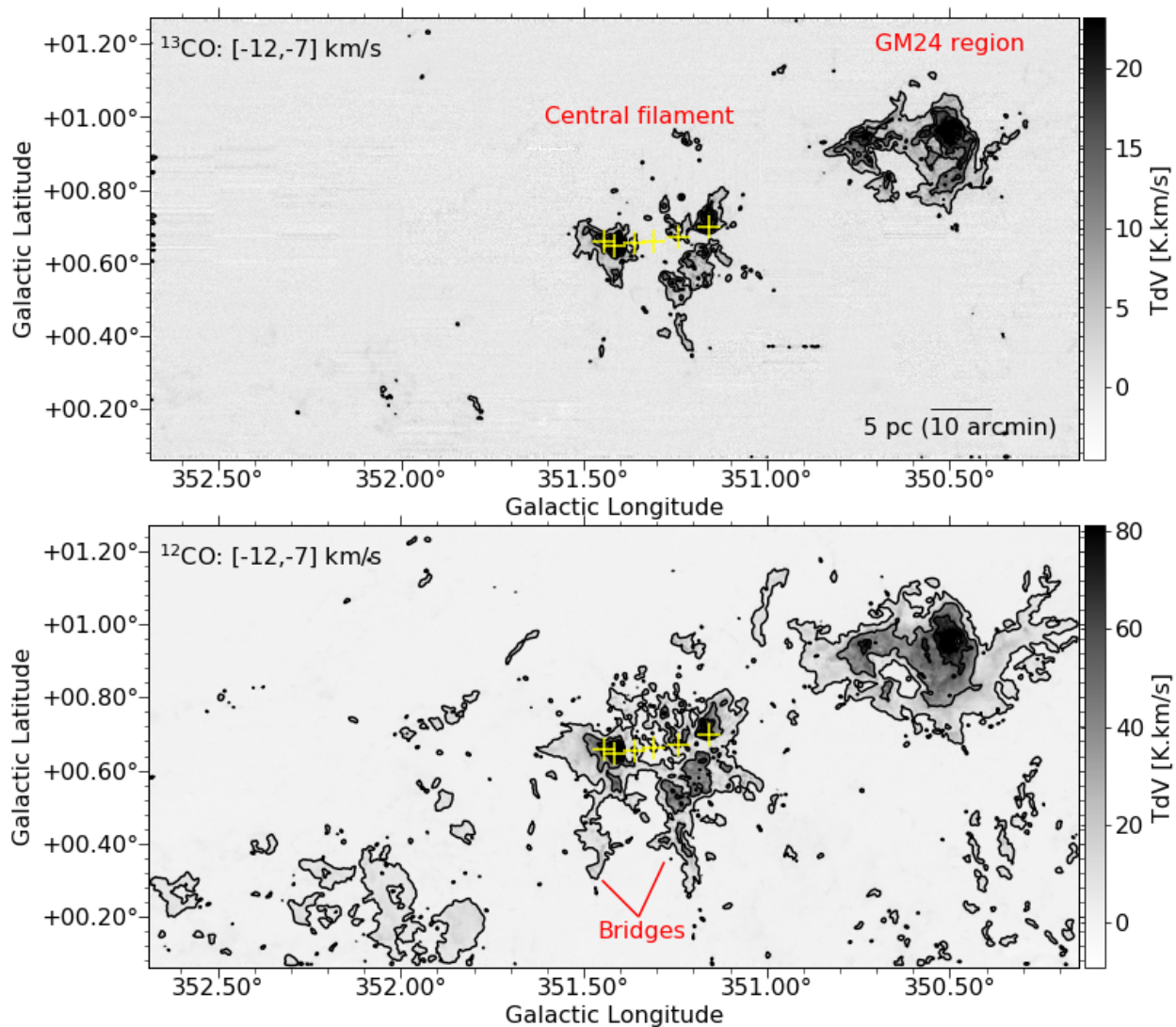


Fig. 17: Maps of ^{13}CO (top) and ^{12}CO (bottom) integrated over the velocity range from -12 to -7 km s^{-1} . Labels and markers are the same as in Fig. 4

and velocity structure toward GM-24 region can be explained by the multiple H II bubbles and shell-like structures. In addition, we observe that the larger bubbles located south to the GM-24 region are shaping the filamentary gas emission structure.

5.2.3. Eastern Filament (EF1): a hub-filament in formation?

Filament EF1 is located around $l = 352$ deg and $b = 0.7$ deg (see Figure 6 and C.3). The filament corresponds to the dark lane observed in the infrared three color map in Figure 1 caused by dust absorption. In addition, Arzoumanian et al. (2022) have reported velocity coherent filamentary structure (VCF47) toward this filament.

In the longitude velocity plots, we observe a broad V-shape toward this filament. These velocity fluctuations are accompanied by the intensity fluctuations with phase shift (Fig. 8, bottom panel). The velocity gradient is also visible in the moment 1 map of ^{13}CO (Fig. F.7). We suggest that this is consistent with the global collapse scenario in which gas is infalling toward the filament EF1. This filament harbours a few ATLAS-GAL clumps (see Fig. C.3). The velocity gradient inferred from

the arms of the V-shape is 1.3 $\text{km s}^{-1} \text{pc}^{-1}$. Assuming a free fall velocity corresponding to the observed velocity gradient and extension of V-shape ($R \sim 2$ pc), we estimate that the kinetic mass ($\approx 2R^3 \nabla V^2 / G$) of the filament $\sim 5 \times 10^3 M_{\odot}$. The channel maps in the $[+1, +5]$ km s^{-1} also show multiple gas streams that are more clearly visible in ^{12}CO (Fig. C.3). The global infall and filamentary gas streams in EF1 indicate that this region is a hub-filament system in formation.

5.3. Supersonic velocity dispersion

We observed supersonic dispersion velocities along the dense gas ridge in NGC 6334 filament. At the spatial resolution of our observations (beam size of $20''$), the Mach number, corresponding to σ_v of 0.9 to 3.0 km s^{-1} are 3 to 11, values inferred from sound speed at an average temperature of 20 K. Supersonic velocity dispersions are commonly observed toward giant filaments (see review by Hacar et al. 2023). Theories on the origin of the velocity dispersion in molecular clouds and filaments are under intense discussion both in theoretical and observational studies if it reflects the gravitational or turbulent origin

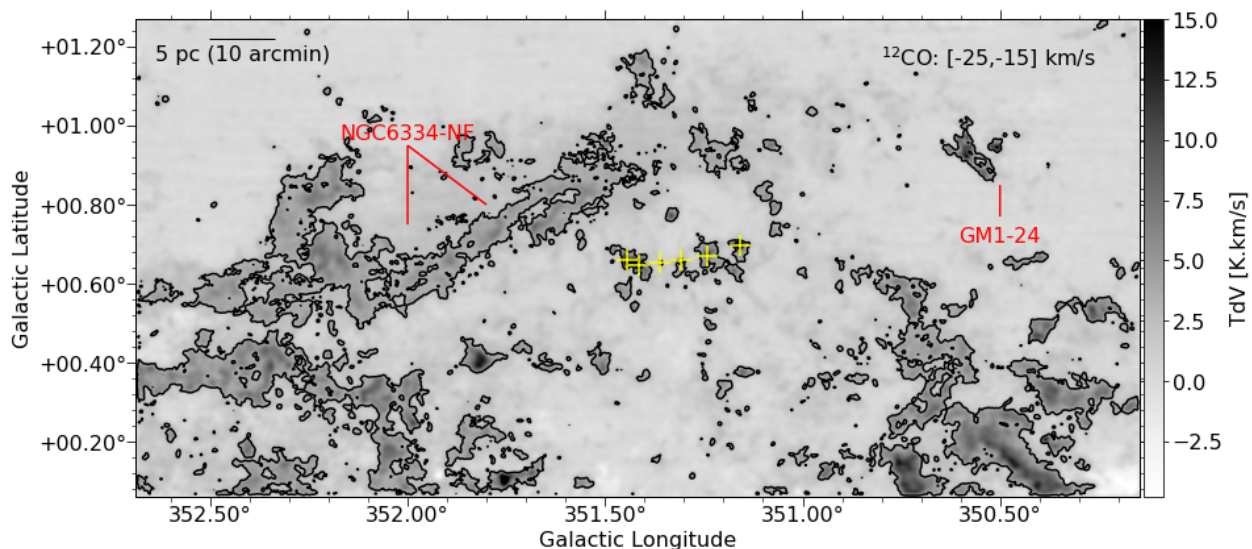


Fig. 18: Map of ^{12}CO integrated emission integrated over the velocity range from -25 to -15 km s^{-1} the contour line representing the 5σ level. The emission north to the NGC 6334 central region is labelled as the northern filament (NF). Yellow plus markers denote the FIR-sources (I[N], I to V from east to west) in the central filament.

(e.g., Ballesteros-Paredes et al. 2011; Heitsch 2013; Arzoumanian et al. 2013; Smith et al. 2016; Clarke et al. 2017; Mattern et al. 2018; Xu et al. 2019; Vázquez-Semadeni et al. 2019; Hacar et al. 2023).

Observationally, it is clear that determinations of velocity dispersions depend on the spatial resolution. Resolved clouds and filaments seem to exhibit dispersions close to the sonic speed (e.g., Hacar & Tafalla 2011; Arzoumanian et al. 2013). In NGC 6334 itself, high resolution observations with ALMA have revealed subsonic and transonic velocity dispersions in filaments and cores (NGC 6334S: Li et al. 2020, NGC 6334 I[N] and I: Sadaghiani et al. 2020). Hacar et al. (2023) investigated relations between velocity dispersion, filament length and line mass and showed that these scaling relations are followed by various types of filaments, which indicates that at larger scales non-thermal motions govern the gas dynamics. Whether the non-thermal motions originate from a turbulence cascade, core forming flows in the filament, global gravitational collapse or cloud collisions requires further investigation.

5.4. Role of H II regions in the star formation processes in NGC 6334 extended region

Various feedback processes act upon molecular clouds, providing mechanical and radiative energy input. Supernova explosions of dying high-mass stars ($> 8M_{\odot}$), stellar winds, stellar jets and outflows provide mechanical feedback while ionizing and non-ionizing radiation provide radiative energy inputs (Klessen & Glover 2016). Toward the NGC 6334 region, only one supernova remnant (G351.7+0.8) has been detected (Green 2019), which is located North-East of the central filament. However, based on optical extinction data, the distance of this supernova remnant was found to be 3.4 kpc (Wang et al. 2020), twice the accepted distance to NGC 6334 (~ 1.7 kpc; Russeil et al. 2012). A large number of OB stars and the H II regions/bubbles created by them drive the feedback in the NGC 6334 extended region.

As shown in Figure 1, OB stars are clustered in the GM-24 region while they are found in association in the NGC 6334 central region (see Russeil et al. 2020). A total of 42 H II re-

gions/bubbles are found in the extended region that are visually identified in the mid-infrared with varying sizes from 0.2 to 12 pc (Anderson et al. 2014). At least eight H II regions, associated with present star formation, are found in and around the NGC 6334 central ridge (see Persi & Tapia 2008). The GM-24 region has bubbles within bubbles (see Figure 1). Only a few H II regions, mostly of smaller size, are found toward the eastern filaments (near EF1, EF2 and G352.5, see Figure 1, 10). Of the 42 H II regions from Anderson et al. (2014), most H II regions (40 of 42) show gas velocities derived from ^{13}CO that are consistent with the velocity of the bulk gas emission (see Table 1). This confirms that they are indeed part of the NGC 6334 region. From a visual inspection of the channel maps of the CO emission structure around the H II regions also using quantitative methods, we find that a significant fraction ($>80\%$) of H II regions have an impact on the surrounding gas. Impact here either means clear shell-like/arc-like structure in emission morphology and/or high-contrast values in the CO intensities at bubble edges. Visually, clear signatures of H II bubbles interacting with the filamentary structure are seen toward GM-24 region in which filaments extending west from the central ridge pass through the edges of the bubbles (see Figure 1 and 10). We suggest that these bubbles, typically larger in size, have induced accumulation of gas in the filament and reached pressure equilibrium conditions with the environment. Barnes et al. (2020) have reported that the maximum size of an H II region is set by pressure equilibrium with the ambient ISM, consistent with our interpretation. Similar to our findings, the role of H II bubbles in the formation of a molecular filament has also been suggested for the case of RCW 120 (Zavagno et al. 2020).

Hundred and sixty-seven ATLASGAL clumps are found in the extended NGC 6334 region, most of which are embedded in the filamentary structure. We searched for their location to investigate possible associations with the H II bubbles. A total of 56 (of 167) ATLASGAL clumps are located on the edges of the H II bubbles ($0.8-1.2 \times R_{\text{HII}}$). We also found that 26 of 42 H II regions have at least one ATLASGAL clump located at the bubble radii. This result hints that H II regions may play an important role in formation of the filaments in which the ATLASGAL clumps are

embedded. Elmegreen 1998 has highlighted the important role of the H II region in the formation of stars at their edges/shells (see also Inutsuka et al. 2015). Cases of positive feedback from H II bubbles are reported towards multiple star forming regions, for example, toward the G305 complex ‘collect and collapse’ model of triggered star formation is reported by Mazumdar et al. (2021).

6. Summary

We conducted observations of the ^{13}CO and ^{12}CO 3 \rightarrow 2 molecular lines toward the extended NGC 6334 filament using the LAsMA instrument on the APEX telescope, with a spectral resolution of 0.25 km s^{-1} and a spatial resolution of ~ 20 arcsec (0.16 pc at 1.7 kpc). In this paper, we focused on studying the emission morphology and velocity structure of the gas in the filament traced by carbon monoxide. The results are summarized here:

- The CO traced gas in the NGC 6334 extended region is filamentary, and extends over 80 pc parallel to the Galactic plane. The central NGC 6334 filament exhibits bright CO emission tracing the dense gas reservoir that extends over 10 pc scale. While ^{13}CO traces denser regions, ^{12}CO exhibits a more extended emission morphology.
- We fitted the ^{13}CO line profiles using an automated Gauss fit algorithm Gausspyplus. Multiple velocity components were required to fit the observed line profiles toward the denser regions indicating the complex gas velocity structure of the filament. Overall, NGC 6334 exhibits two distinct gas components at velocities -3.9 and -9.2 km s^{-1} . A third component at $\sim -20 \text{ km s}^{-1}$ is kinematically connected to the extended region.
- We observed velocity and intensity fluctuations (so called ‘wiggles’) along the dense ridge of the filament. We suggest that such fluctuations are likely to be associated with the local density enhancements and gravitational infall onto the filament.
- We found that the dense gas along the filament shows velocity dispersions of $2 > \sigma_v > 0.9 \text{ km s}^{-1}$. Higher velocity dispersions ($> 2 \text{ km s}^{-1}$) were observed toward NGC 6334 central filament and an Eastern Filament (EF1). The velocity dispersion in NGC 6334 filament is supersonic at the spatial resolution of our observations.
- We investigated the molecular gas structure around the infrared H II regions identified by Anderson et al. (2014) using azimuthally averaged radial ^{13}CO intensity profiles and measured the line intensity enhancement using the contrast method. Toward most H II regions, we detected molecular line emission and reported the systemic velocities. We found 36 of 42 H II regions to show the signature of molecular gas clearance from the center. These sources exhibit little emission or a flat emission profile toward the central region with an intensity increasing outward or a bumpy feature near or at the H II radii. Using a contrast measurement method, we found intensity enhancements toward 34 of 42 H II regions. In addition, we found that many H II regions (26 of 42) have at least one ATLASGAL clump located at their shell radii.
- A visually clear signature of H II bubble shells emanating from the filamentary structure is observed in particular toward the GM-24 region, in which filaments extending west from the central ridge are located on the edges of the bubbles. We suggest that these bubbles, typically evolved and larger in size, have assisted the formation of gas filament by accumulating gas at their edges and have reached pressure equilibrium with the environment.
- We investigated the gas velocity structure around six FIR sources (I[N], I to V) in the central NGC 6334 filament using position velocity diagrams and found evidence for gas compression toward all of them. In addition, we studied the gas velocity structure around H II regions using lv and bv plots in which velocities were obtained from Gauss fitting of ^{13}CO line profiles. Toward a third of the H II regions we observed a V-shape emission indicating multiple gas compression in the NGC 6334 extended filament.
- In the longitude-velocity (lv) plot for the entire mapped region (Figure 8), we observed broad V-shaped (or inverted V-shaped) velocity structure toward NGC 6334 central filament and the eastern filament ($l \sim 352.1$ deg). Toward the NGC 6334 central filament and eastern filament EF1 ($l \sim 352.1$ deg), the velocity gradient inferred from the arms of the V-shapes were consistent with a global infall scenario. We conclude that east filament EF1 ($l \sim 352.1$ deg) is a hub-filament system in formation.
- Finally, we studied the kinematic connection of ‘bridge’ features and the northern filament (NGC 6334-NF) to the main gas component in NGC 6334. We found NGC 6334-NF contains relatively quiescent gas and does not harbour any star forming clumps traced by submillimeter emission from dust. We suggest that the ‘bridge’ features are possibly linked to cloud-cloud collisions in NGC 6334-NF and the NGC 6334 main filament.

In summary, our observations revealed a complex gas velocity structure in the NGC 6334 filament that extends over ~ 80 pc. Located in the west, GM24 region exhibits bubbles within bubbles and is at relatively evolved stage of star formation. The NGC 6334 central ridge is undergoing global gas infall and exhibits two gas ‘bridge’ features possibly indicating cloud-cloud collisions in the NGC 6334-NF and the NGC 6334 main gas component. The relatively quiescent eastern filament (EF1 - G352.1) also shows the kinematic signature of global gas infall onto the filament. We detected molecular emission around most infrared H II regions and found that most H II regions have already cleared out the molecular gas from the center and that many have shell/ring like molecular structure around them. We also observed multiple gas compression signatures around the H II regions and highlighted their important role in shaping the gas emission and velocity structure in the NGC 6334 extended region and in the overall evolution of this star forming complex.

Data availability

The supplementary materials (figures and tables of the Appendix section) are available online at: <https://doi.org/10.5281/zenodo.13642114>.

Acknowledgements. We thank anonymous referee for the constructive feedback that helped to improve the manuscript. This publication is based on data acquired with the Atacama Pathfinder Experiment (APEX) under program ID M-0107.F-9518A-2021. APEX has been a collaboration between the Max-Planck-Institut für Radioastronomie, the European Southern Observatory, and the Onsala Space Observatory. This work was supported by the Collaborative Research Council (CRC) 956, sub-project A6, and CRC 1601, sub projected B1, funded by the Deutsche Forschungsgemeinschaft (DFG). G.G acknowledges support by the ANID BASAL project FB210003.

References

- Anderson, L. D., Bania, T. M., Balsler, D. S., et al. 2014, *ApJS*, 212, 1
 André, P., Revêret, V., Könyves, V., et al. 2016, *A&A*, 592, A54
 Arzoumanian, D., André, P., Peretto, N., & Könyves, V. 2013, *A&A*, 553, A119

- Arzoumanian, D., Russeil, D., Zavagno, A., et al. 2022, *A&A*, 660, A56
- Ballesteros-Paredes, J., Hartmann, L. W., Vázquez-Semadeni, E., Heitsch, F., & Zamora-Avilés, M. A. 2011, *MNRAS*, 411, 65
- Barnes, A. T., Longmore, S. N., Dale, J. E., et al. 2020, *MNRAS*, 498, 4906
- Churchwell, E. 2002, *ARA&A*, 40, 27
- Churchwell, E., Watson, D. F., Povich, M. S., et al. 2007, *ApJ*, 670, 428
- Clarke, S. D., Whitworth, A. P., Duarte-Cabral, A., & Hubber, D. A. 2017, *MNRAS*, 468, 2489
- Duarte-Cabral, A. & Dobbs, C. L. 2016, *MNRAS*, 458, 3667
- Elmegreen, B. G. 1998, in *Astronomical Society of the Pacific Conference Series*, Vol. 148, *Origins*, ed. C. E. Woodward, J. M. Shull, & J. Thronson, Harley A., 150
- Frerking, M. A., Langer, W. D., & Wilson, R. W. 1982, *ApJ*, 262, 590
- Fukui, Y., Kohno, M., Yokoyama, K., et al. 2018a, *PASJ*, 70, S44
- Fukui, Y., Kohno, M., Yokoyama, K., et al. 2018b, *PASJ*, 70, S41
- Green, D. A. 2019, *Journal of Astrophysics and Astronomy*, 40, 36
- Guo, W., Chen, X., Feng, J., et al. 2021, *ApJ*, 921, 23
- Hacar, A., Clark, S. E., Heitsch, F., et al. 2023, in *Astronomical Society of the Pacific Conference Series*, Vol. 534, *Astronomical Society of the Pacific Conference Series*, ed. S. Inutsuka, Y. Aikawa, T. Muto, K. Tomida, & M. Tamura, 153
- Hacar, A. & Tafalla, M. 2011, *A&A*, 533, A34
- Heitsch, F. 2013, *ApJ*, 769, 115
- Henshaw, J. D., Kruijssen, J. M. D., Longmore, S. N., et al. 2020, *Nature Astronomy*, 4, 1064
- Inoue, T. & Fukui, Y. 2013, *ApJ*, 774, L31
- Inutsuka, S.-i., Inoue, T., Iwasaki, K., & Hosokawa, T. 2015, *A&A*, 580, A49
- Jackson, J. M., Rathborne, J. M., Shah, R. Y., et al. 2006, *ApJS*, 163, 145
- Klein, B., Hochgürtel, S., Krämer, I., et al. 2012, *A&A*, 542, L3
- Klessen, R. S. & Glover, S. C. O. 2016, in *Saas-Fee Advanced Course*, Vol. 43, *Saas-Fee Advanced Course*, ed. Y. Revaz, P. Jablonka, R. Teyssier, & L. Mayer, 85
- Kraemer, K. E. & Jackson, J. M. 1999, *ApJS*, 124, 439
- Li, S., Zhang, Q., Liu, H. B., et al. 2020, *ApJ*, 896, 110
- Loughran, L., McBreen, B., Fazio, G. G., et al. 1986, *ApJ*, 303, 629
- Mattern, M., Kauffmann, J., Csengeri, T., et al. 2018, *A&A*, 619, A166
- Mazumdar, P., Wyrowski, F., Urquhart, J. S., et al. 2021, *A&A*, 656, A101
- Muñoz, D. J., Mardones, D., Garay, G., et al. 2007, *ApJ*, 668, 906
- Persi, P. & Tapia, M. 2008, in *Handbook of Star Forming Regions, Volume II*, ed. B. Reipurth, Vol. 5, 456
- Riener, M., Kainulainen, J., Henshaw, J. D., et al. 2019, *A&A*, 628, A78
- Russeil, D., Adami, C., Bouret, J. C., et al. 2017, *A&A*, 607, A86
- Russeil, D., Schneider, N., Anderson, L. D., et al. 2013, *A&A*, 554, A42
- Russeil, D., Tigé, J., Adami, C., et al. 2016, *A&A*, 587, A135
- Russeil, D., Zavagno, A., Adami, C., et al. 2012, *A&A*, 538, A142
- Russeil, D., Zavagno, A., Nguyen, A., et al. 2020, *A&A*, 642, A21
- Sadaghiani, M., Sánchez-Monge, Á., Schilke, P., et al. 2020, *A&A*, 635, A2
- Smith, R. J., Glover, S. C. O., Klessen, R. S., & Fuller, G. A. 2016, *MNRAS*, 455, 3640
- Smith, R. J., Treß, R. G., Sormani, M. C., et al. 2020, *MNRAS*, 492, 1594
- Tigé, J., Motte, F., Russeil, D., et al. 2017, *A&A*, 602, A77
- Tremblin, P., Minier, V., Schneider, N., et al. 2013, *A&A*, 560, A19
- Urquhart, J. S., Koenig, C., Giannetti, A., et al. 2018a, *VizieR Online Data Catalog*, J/MNRAS/473/1059
- Urquhart, J. S., König, C., Giannetti, A., et al. 2018b, *MNRAS*, 473, 1059
- van der Tak, F. F. S., Black, J. H., Schöier, F. L., Jansen, D. J., & van Dishoeck, E. F. 2007, *A&A*, 468, 627
- Vázquez-Semadeni, E., Palau, A., Ballesteros-Paredes, J., Gómez, G. C., & Zamora-Avilés, M. 2019, *MNRAS*, 490, 3061
- Wang, S., Zhang, C., Jiang, B., et al. 2020, *A&A*, 639, A72
- Wilson, T. L. & Rood, R. 1994, *ARA&A*, 32, 191
- Xu, S., Ji, S., & Lazarian, A. 2019, *ApJ*, 878, 157
- Zavagno, A., André, P., Schuller, F., et al. 2020, *A&A*, 638, A7
- Zernickel, A., Schilke, P., & Smith, R. J. 2013, *A&A*, 554, L2
- Zhou, J. W., Wyrowski, F., Neupane, S., et al. 2023, *A&A*, 676, A69

Appendix A: rms noise and Gaussian components: ^{13}CO (3-2)

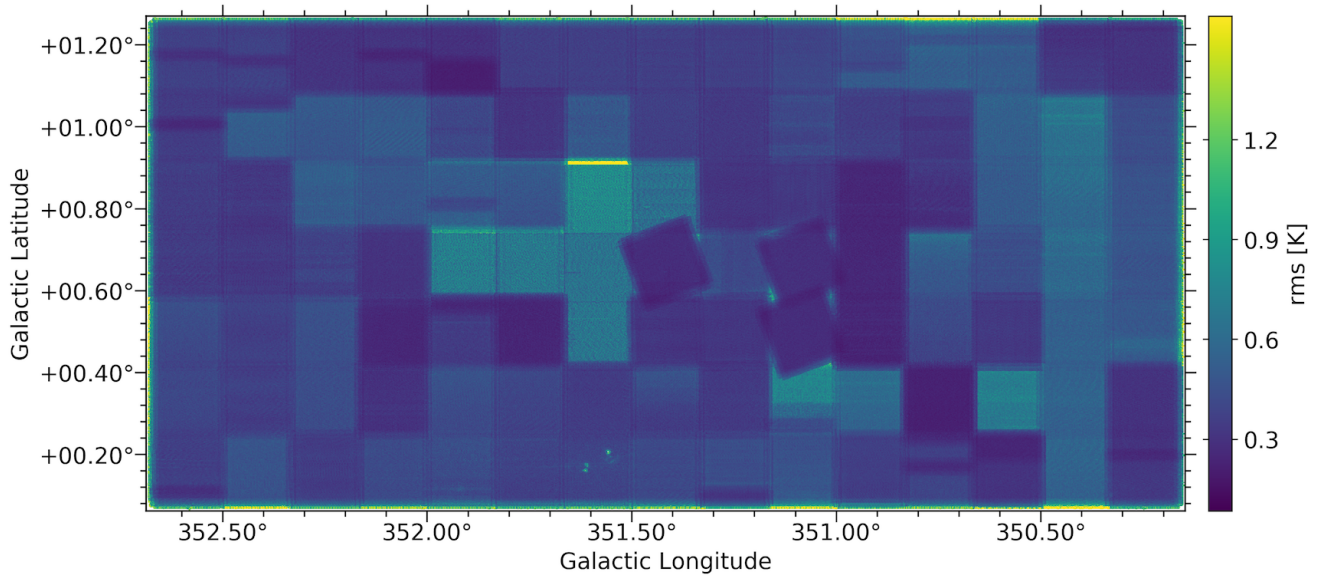


Fig. A.1: rms noise map of ^{13}CO toward the NGC 6334 mapped region.

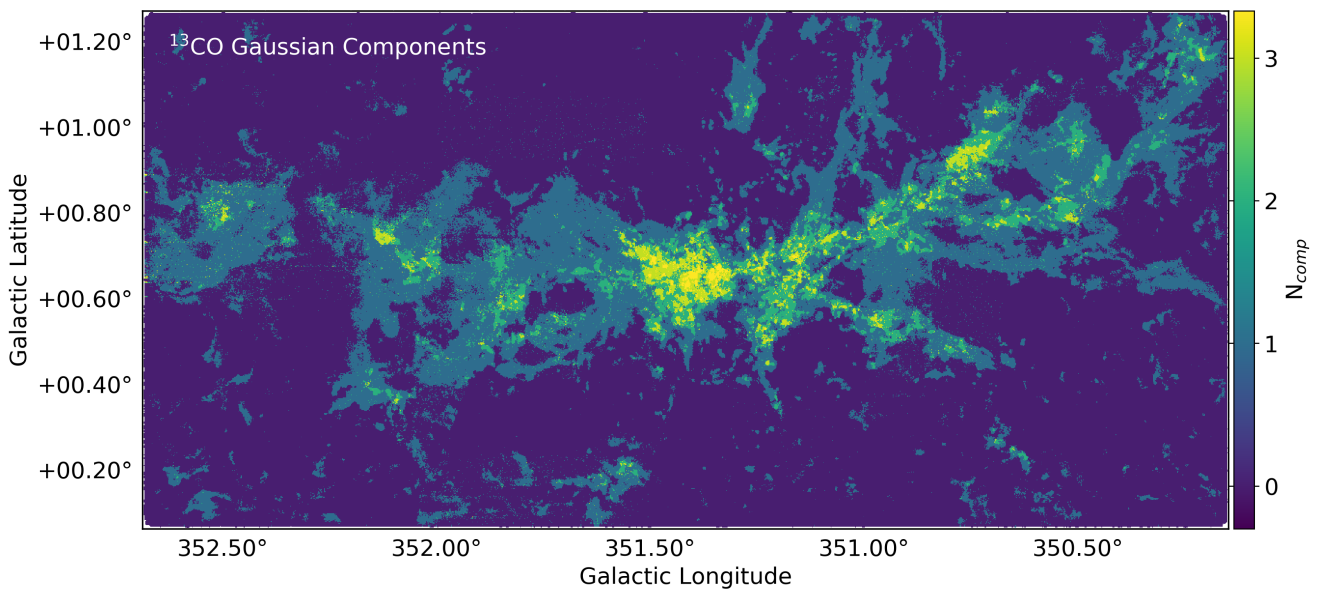


Fig. A.2: Number of Gauss components per pixel fitted to the ^{13}CO line profile toward the NGC 6334 region.

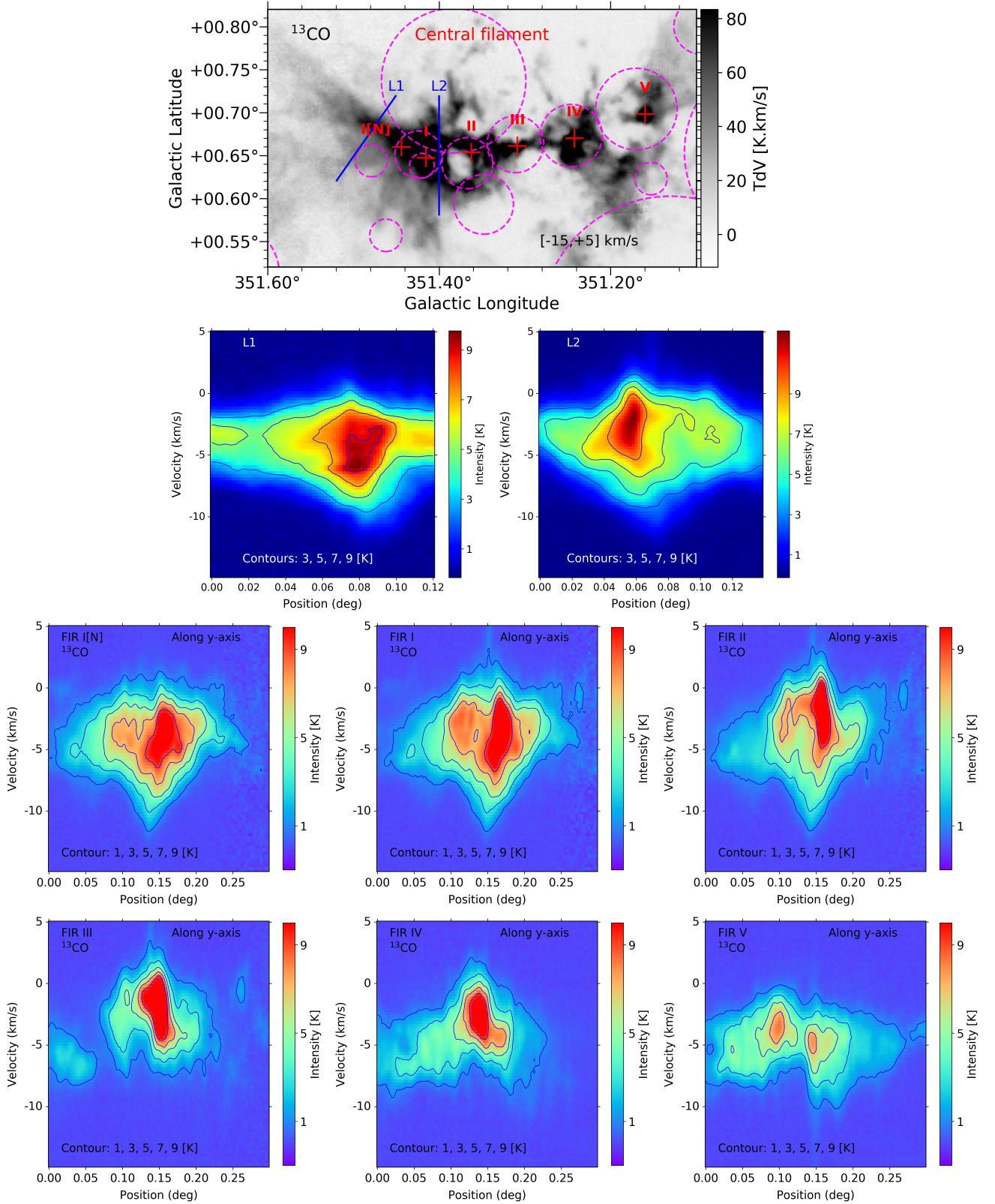
Appendix B: PV maps toward selected regions and FIR sources in the NGC 6334 central filament


Fig. B.1: Position velocity maps (bottom panels) toward three selected slices (L1 and L2 indicated in top panel) perpendicular to the central filament and toward FIR-sources (I[N], I to V indicated by red plus markers in top panel) along y-axis (latitude). Magenta circles indicate H II regions from [Anderson et al. 2014](#). The slices L1 and L2 show same regions, MFS cold and MFS warm, presented in Figure 12 of [Arzoumanian et al. 2022](#).

Appendix C: Channel maps of selected regions

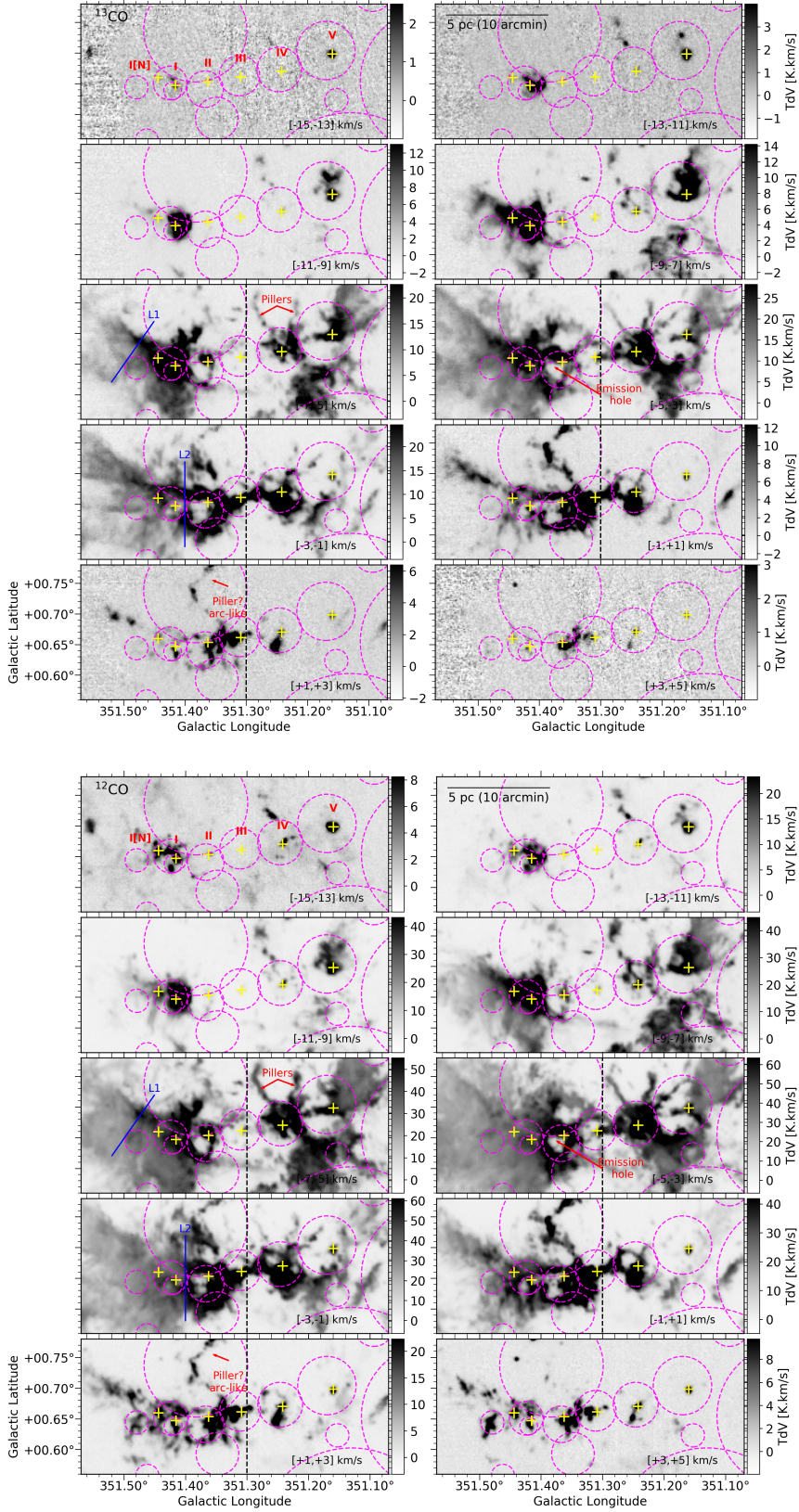


Fig. C.1: Channel map of ^{13}CO and ^{12}CO toward NGC 6334 central filament region. The vertical dotted line indicates the longitude where we observe the V shape in the lv plot (in Fig 14). Magenta/red circles indicate H II regions from Anderson et al. (2014). Blue lines indicate along which the pv-maps are shown in Fig. B.1.

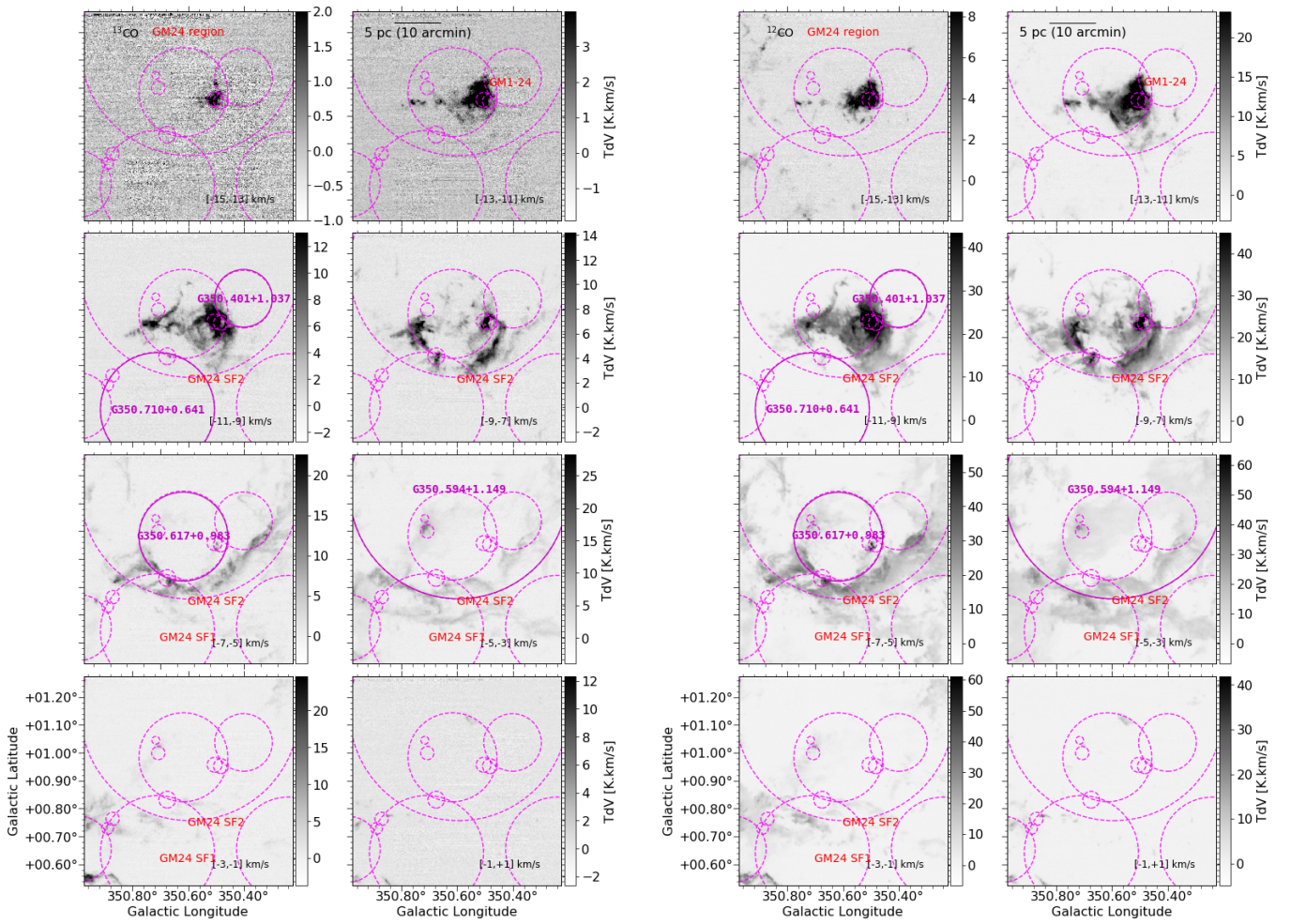


Fig. C.2: Channel map of ^{13}CO and ^{12}CO toward GM-24 region. Magenta/red circles indicate H II regions from Anderson et al. (2014).

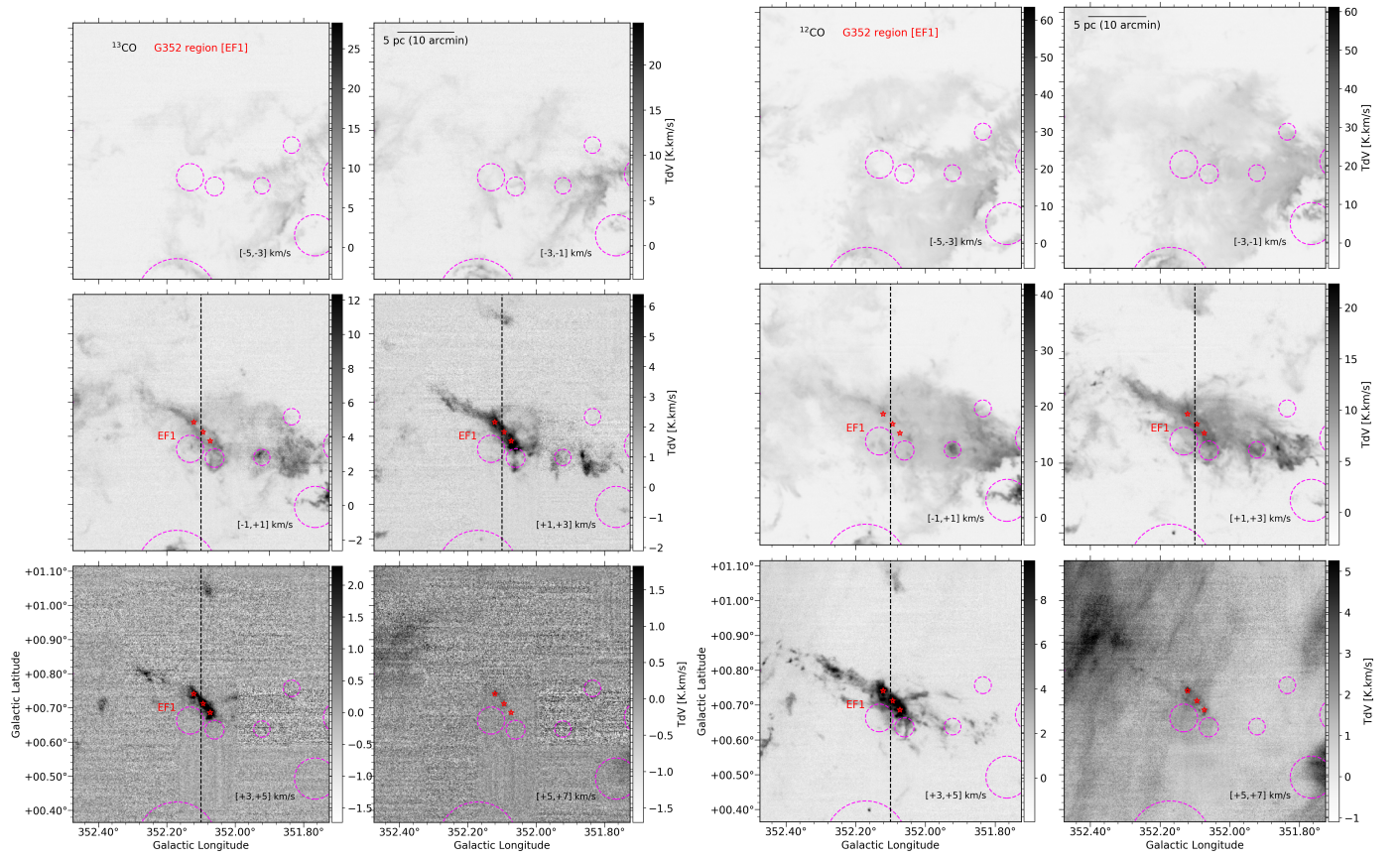


Fig. C.3: Channel map of ^{13}CO and ^{12}CO toward G352.1 region. The vertical dotted line indicates the longitude where we observe the V shape in the lv plot. Magenta circles indicate H II regions from Anderson et al. (2014). Red star symbols show the location of ATLASGAL clumps found in the filament.

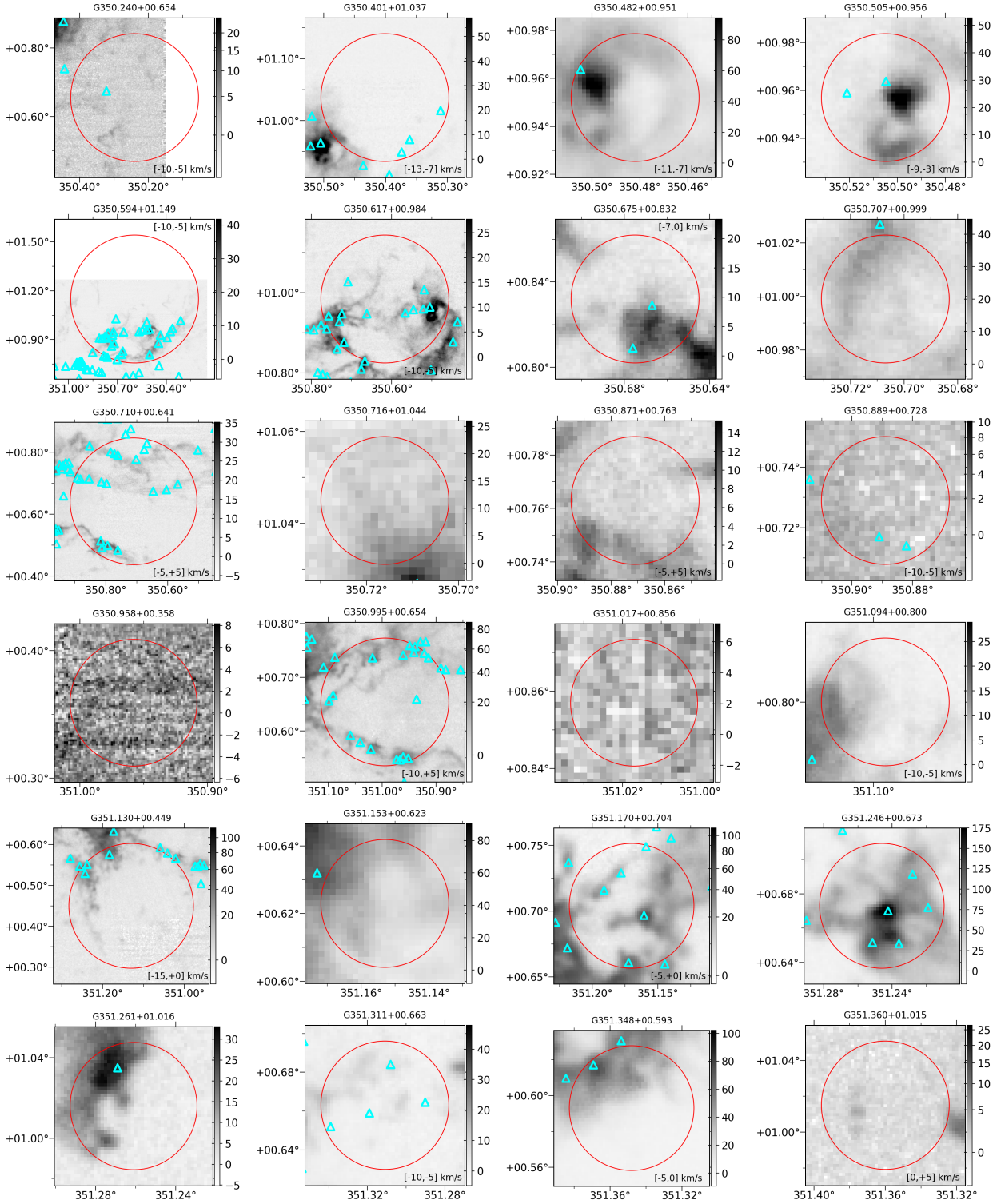
Appendix D: ^{13}CO emission maps of H II regions

Fig. D.1: ^{13}CO emission maps of H II regions integrated over -15 to $+5 \text{ km s}^{-1}$, otherwise indicated inside each maps. Color wedges indicate TdV in K km s^{-1} . Cyan triangles indicate positions of the ATLASGAL clumps.

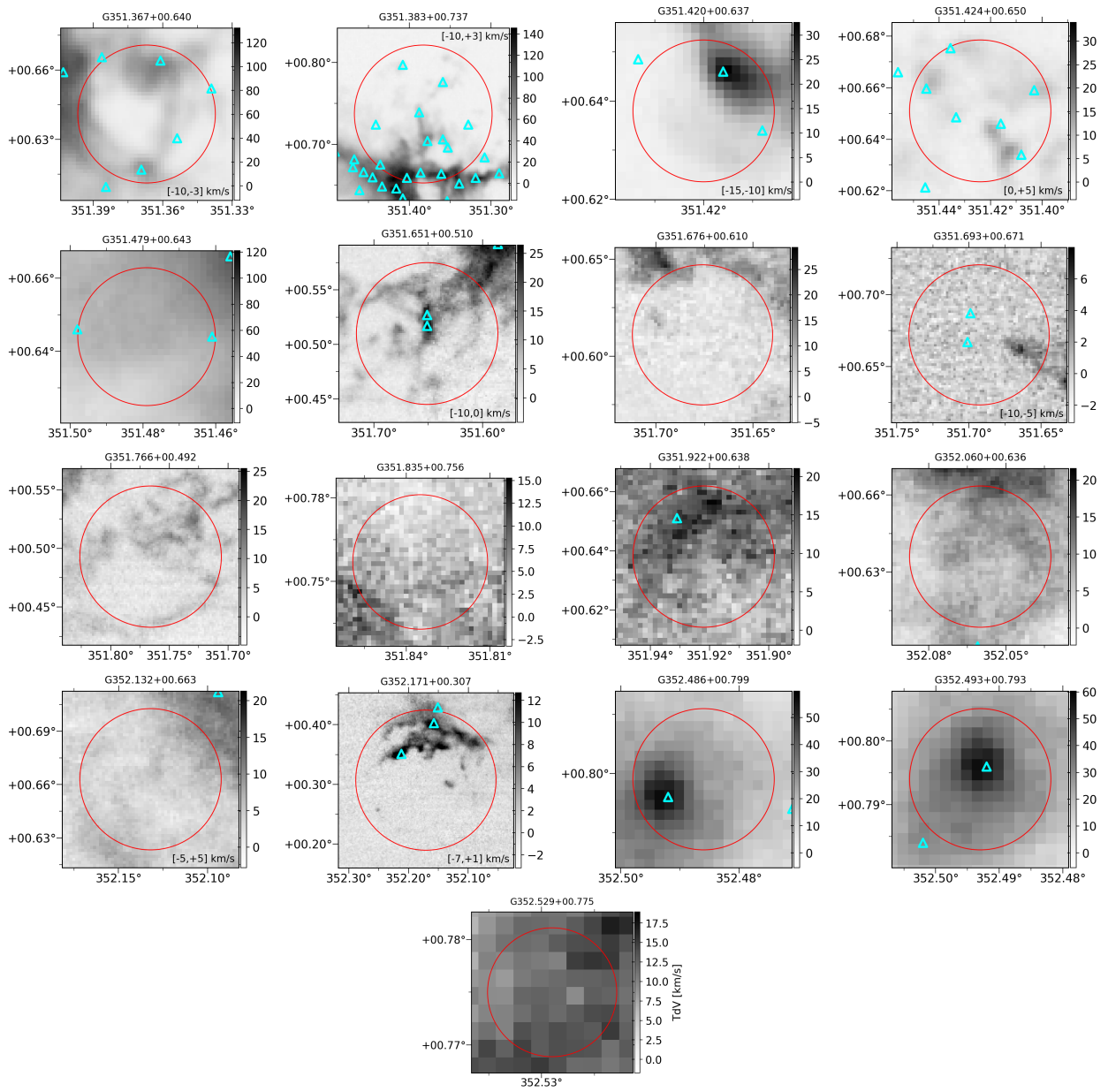


Fig. D.2: Same as Figure D.1

Appendix E: Radial profiles and contrast parameter

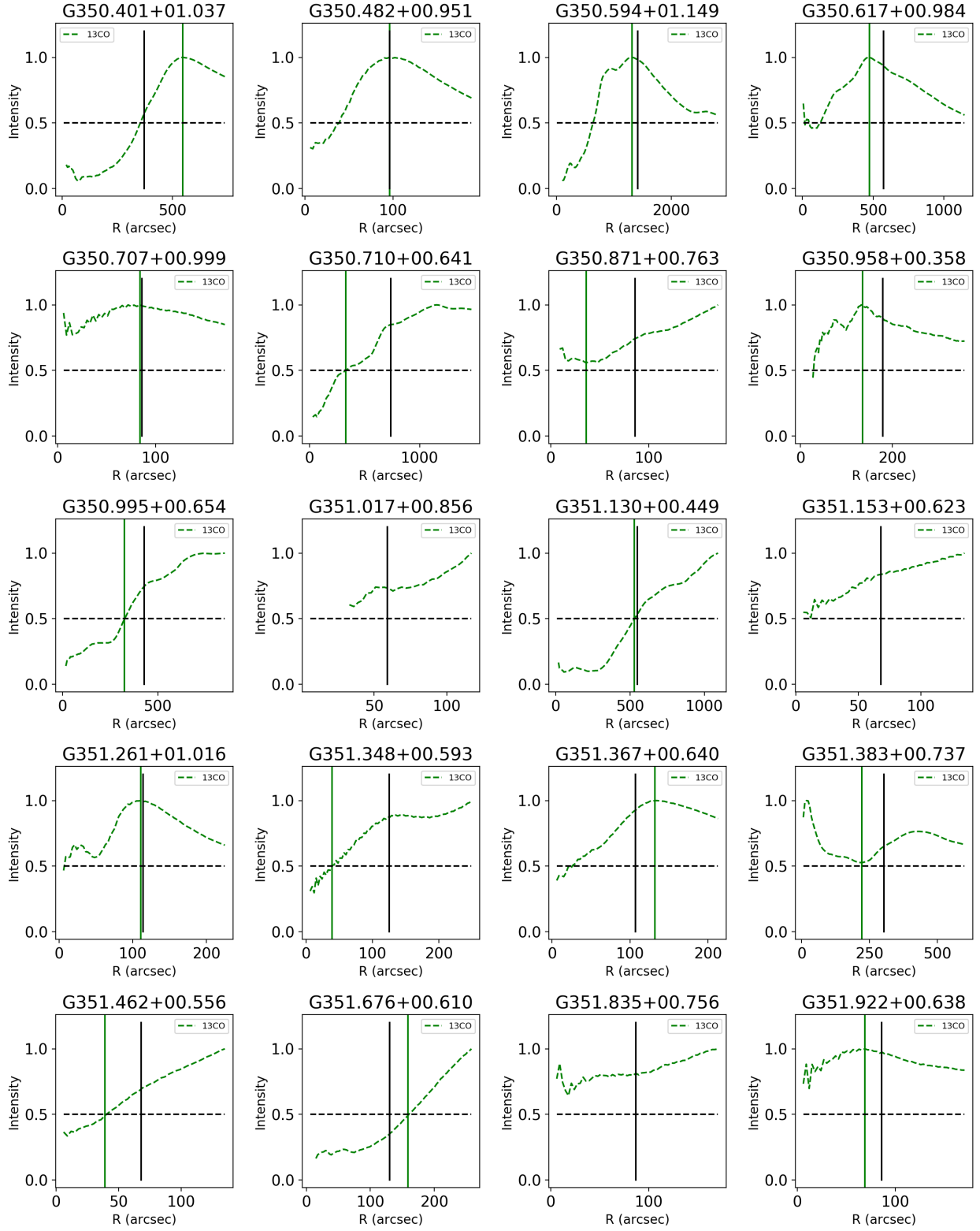


Fig. E.1: Azimuthally averaged ^{13}CO emission profiles (shown in green color) toward H II regions exhibiting increasing radial intensity profiles, with or without the shell/ring like features, computed from velocity range -15 to $+5$ km s^{-1} . Vertical black line indicate the radii from Anderson et al. 2014 and vertical green line indicate sizes estimated from ^{13}CO emission profiles. Horizontal black line indicates 50% value of the intensity maxima.

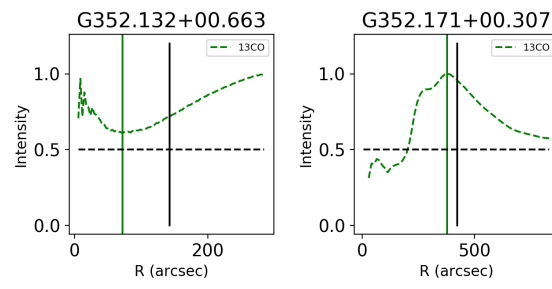


Fig. E.2: Same as Fig. E.1.

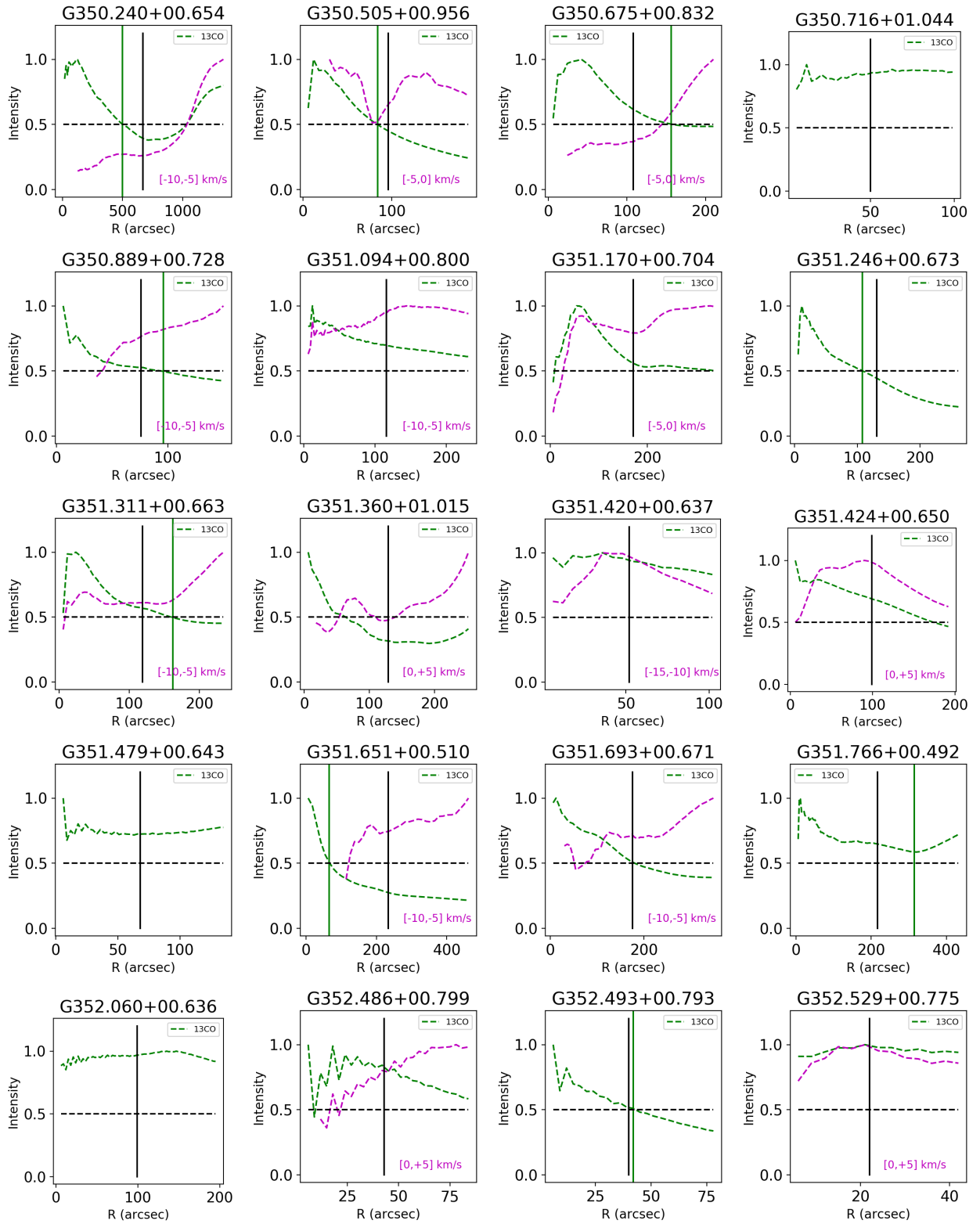


Fig. E.3: Same as Fig. E.1 for H II regions exhibiting centrally peaked emission with decreasing intensity profiles or flat radial profiles. In addition, magenta radial line profiles are shown for particular velocity ranges labelled at the bottom left corner of each plots.

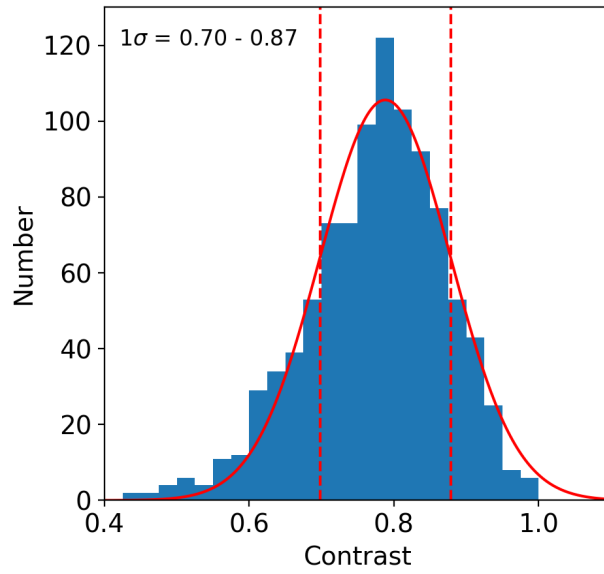


Fig. E.4: Contrast values of 1000 randomly sampled shells/rings obtained from ^{13}CO moment map for velocity ranges -15 to $+5$ km s^{-1} and radii $0.6R$ to $1.2R$, where R is radius of randomly selected region. The radius of randomly created rings range from $20''$ to $700''$, similar to the sizes of H II regions found in NGC 6334 extended region. 1σ range of contrast values are indicated by the dotted red lines.

Appendix F: Longitude-velocity (lv) and latitude-velocity (bv) plots

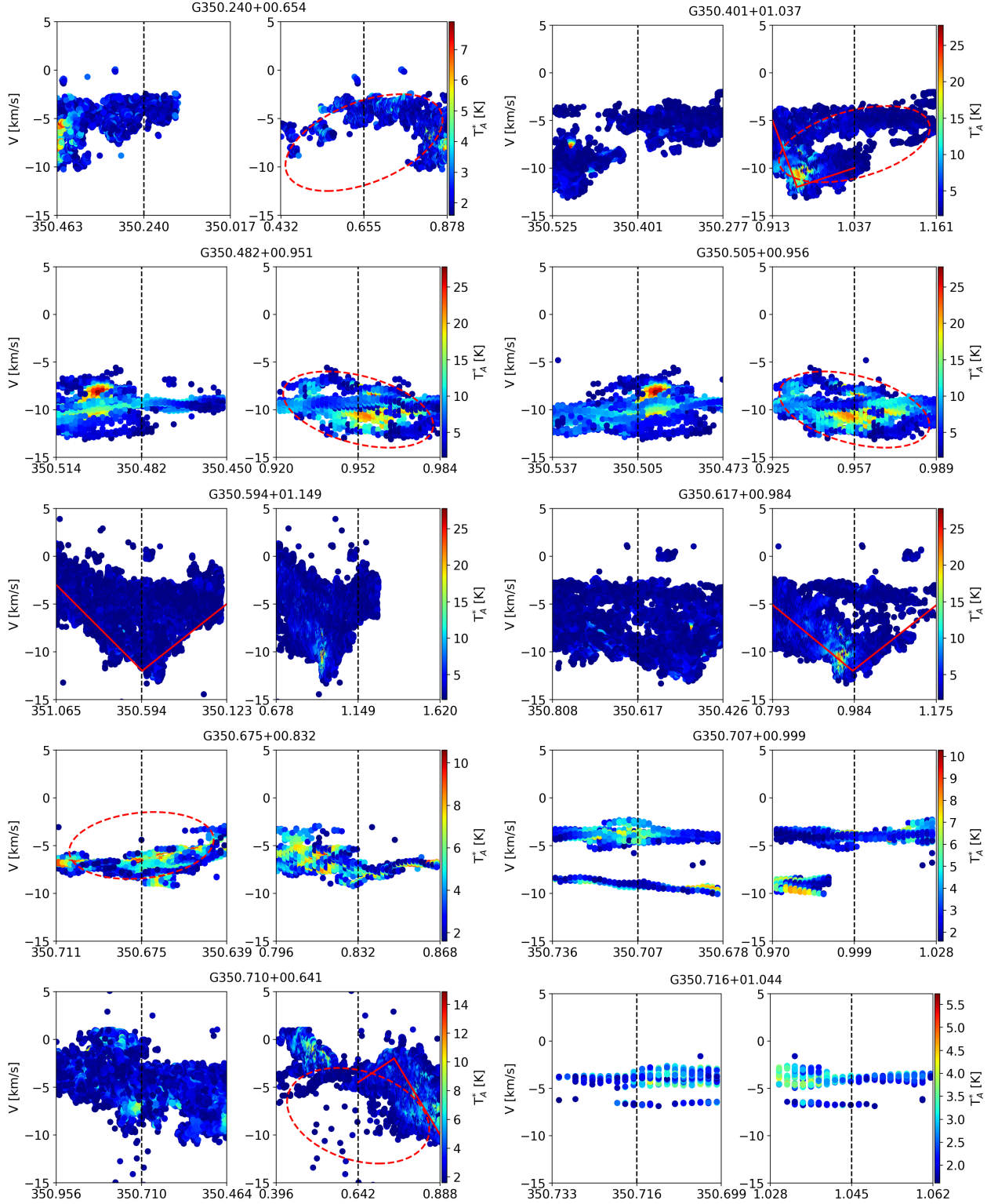


Fig. F.1: Longitude-velocity (lv) and latitude-velocity (bv) plots toward the H II sources. Color bars shows Gaussian peak intensity (T_A^* [K]). Ellipse in red color (if present) indicate visual fit to the velocity structure to infer expansion velocities. Red lines are used to indicate tentative V-shapes in the velocity structure. Name of the H II regions are given on top of each pair of maps.

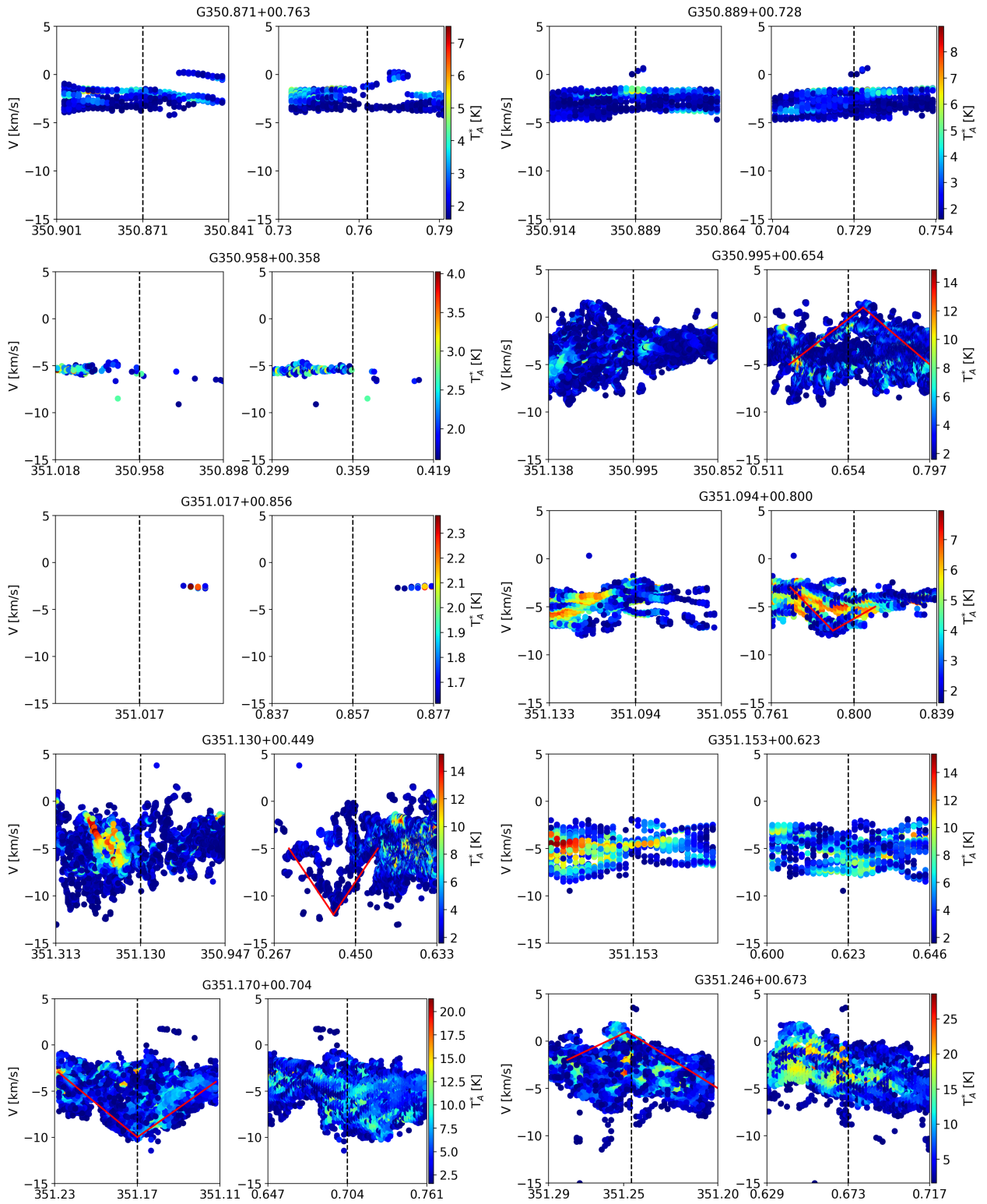


Fig. F.2: Same as Figure F.1

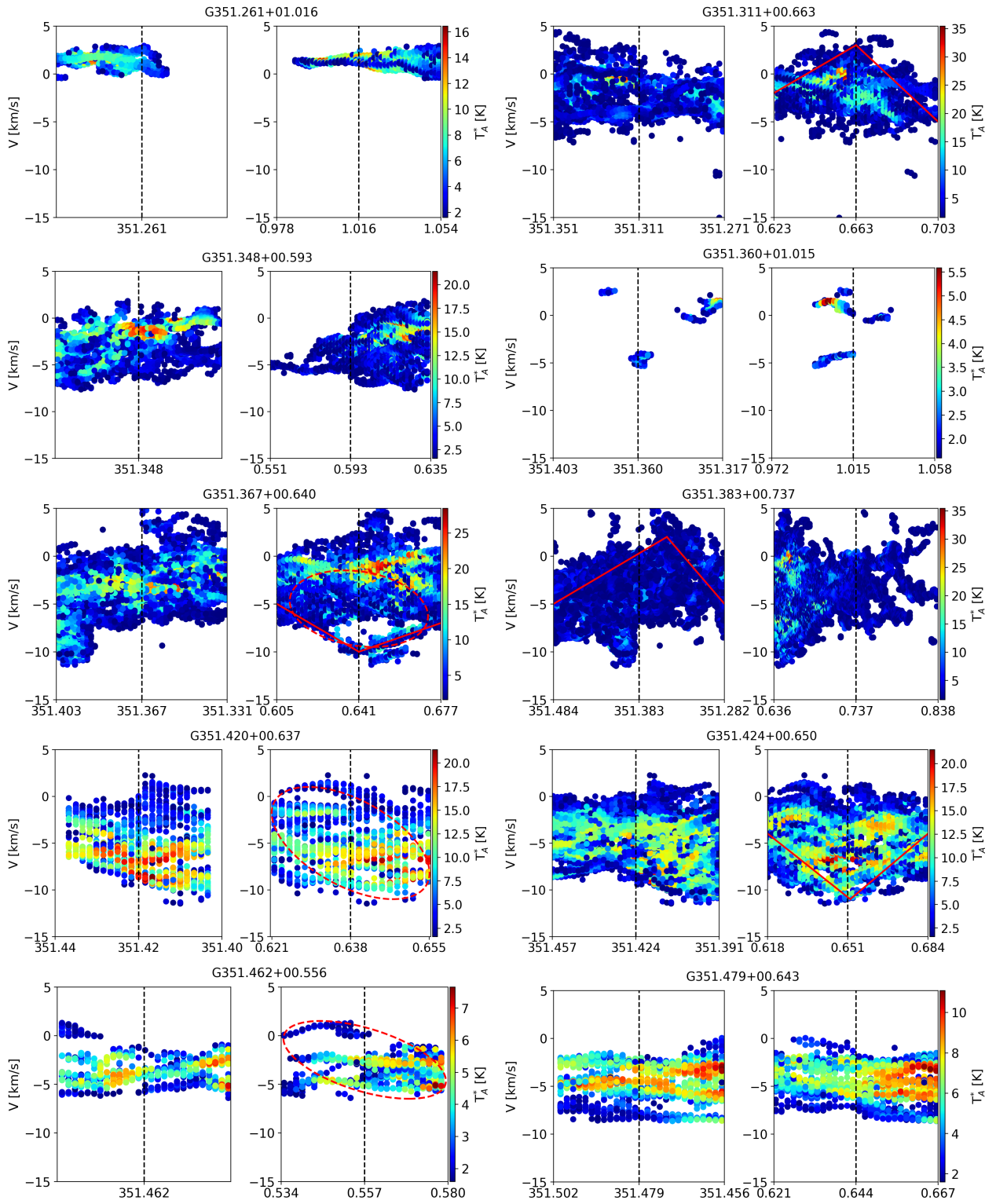


Fig. F.3: Same as Figure F.1

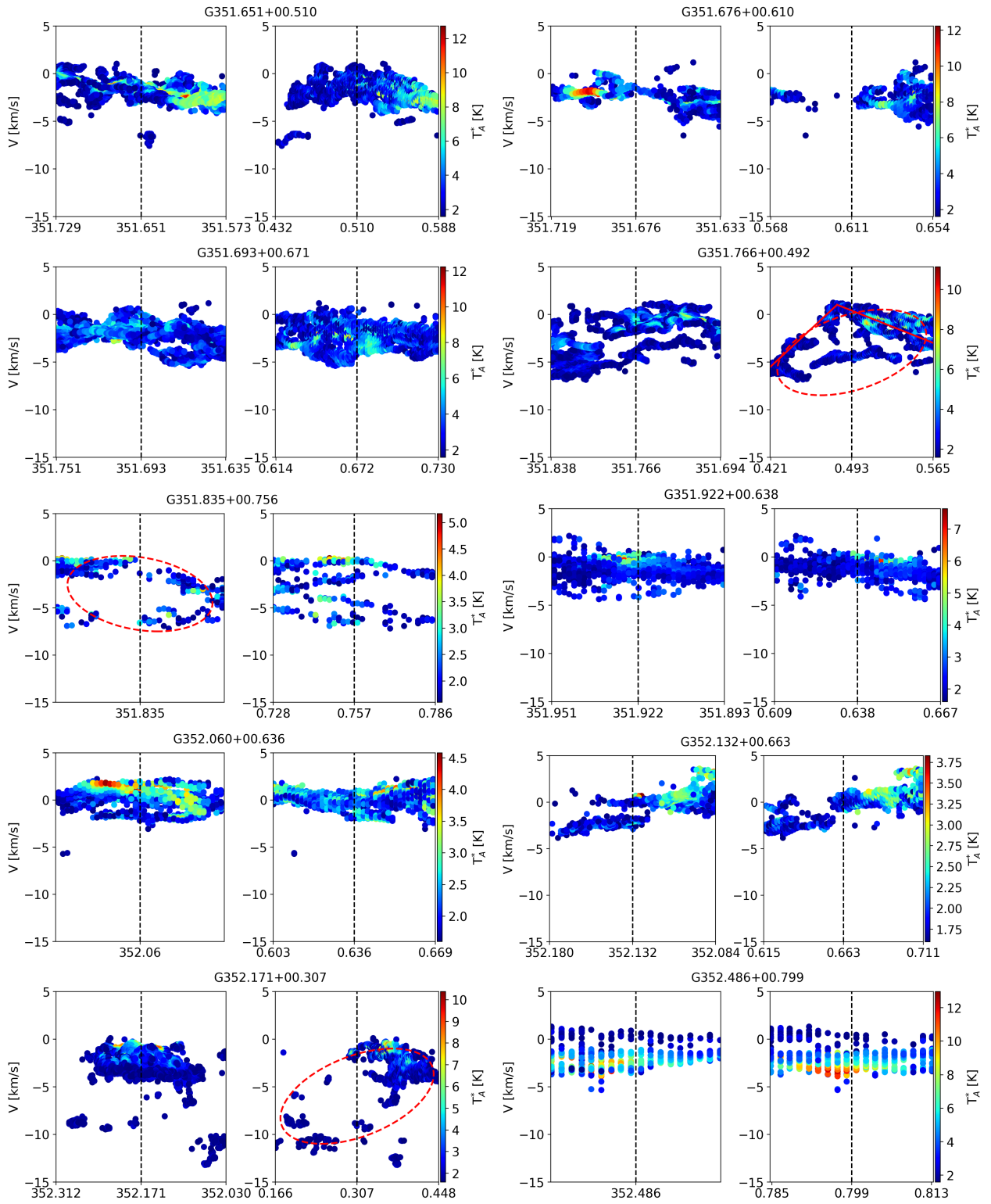


Fig. F.4: Same as Figure F.1

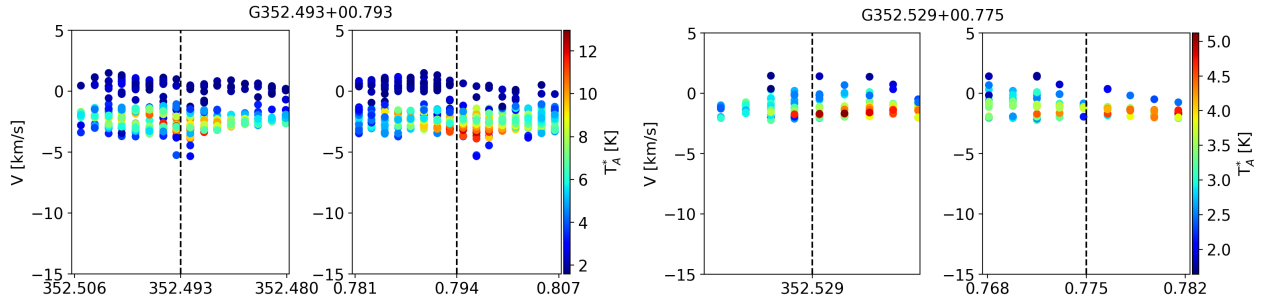


Fig. F.5: Same as Figure F.1

Table F.1: Expansion velocities (V_{exp}) of the H II regions derived from an elliptical fit to the lv or bv plots.

H II region	Fit parameters (x, y, D1, D2, θ)	V_{exp} [km s $^{-1}$]
G350.240+00.654	0.655, -7.5, 0.372, 10, -65	5.0
G350.401+01.037	1.037, -7.5, 0.207, 8, -40	4.0
G350.482+0.952	0.952, -10, 0.053, 8, 10	4.0
G350.505+0.957	0.957, -10, 0.053, 8, 10	4.0
G350.675+0.832	350.675, -5, 0.060, 7, 5	3.5
G350.71+0.642	0.642, -8, 0.408, 10., 40	5.0
G351.367+0.641	0.641, -5.5, 0.059, 8, 5	4.0
G351.42+0.638	0.638, -5, 0.029, 12, 5	4.0
G351.462+0.557	0.557, -2.5, 0.038, 8, 10	4.0
G351.766+0.493	0.493, -4, 0.120, 9, -20.	4.5
G351.835+0.757	351.835, -3.5, 0.048, 8, -5	4.0
G352.171+0.307	0.307, -6, 0.235, 10, -40	5.0

Notes. Fit parameters (central position in [l,v] or [b,v], diameter in x-axis [deg], diameter in y-axis [km/s] and position angle [deg]) are given in Col.2. Derived expansion velocities V_{exp} in km/s are given in Col. 3.

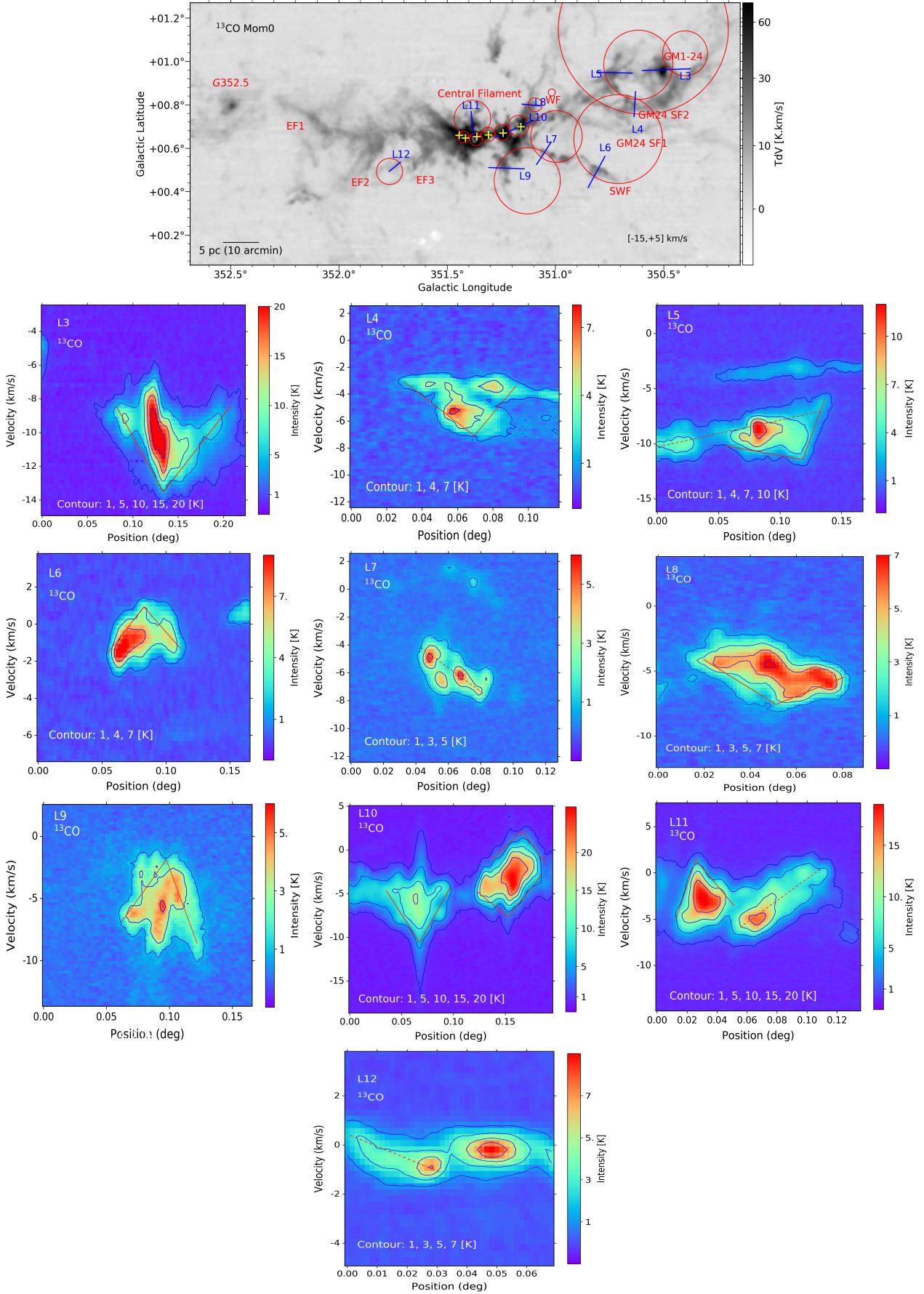


Fig. F.6: Top: ^{13}CO moment0 map. H II regions that show signature of V-shaped velocity structure in Fig F.1 to F.5 are shown in red circles. Blue lines from L3 to L12 indicate the slices in which PV maps are constructed with widths of three beam size (0.016 deg). Bottom panels: PV maps along the blue lines indicated in the top panel image. Observed V-shaped velocity structure (red lines) and velocity gradient (dotted red lines) are indicated in each maps.

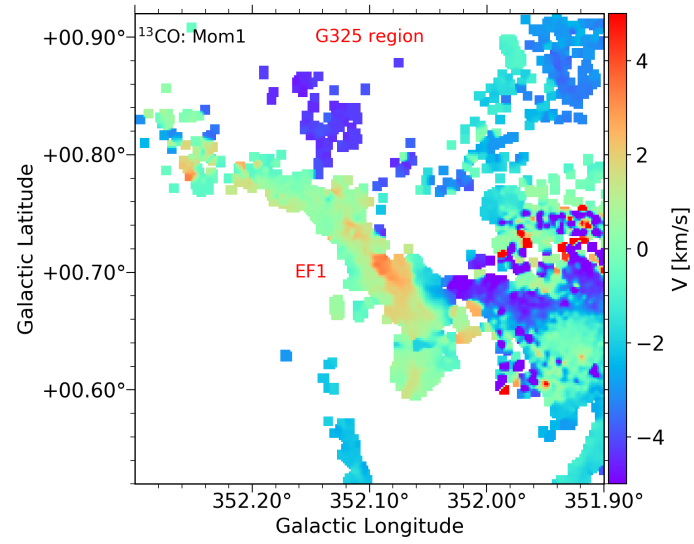


Fig. F.7: ^{13}CO moment one map toward G352 region (EF1). The velocity gradient in hub-filament candidate EF1 filament is clearly observable.